Experimental Investigations of Solid-Solid Thermal Interface Conductance

MASSACHUSETTS INSTITUTE
OF TECHNOLOGY
SEP 0 1 2010
LIBRARIES
ARCHIVES

by

Kimberlee Chiyoko Collins

Submitted to the Department of Mechanical Engineering
in partial fulfillment of the requirements for the degree of

Master of Science in Mechanical Engineering

at the

MASSACHUSETTS INSTITUTE OF TECHNOLOGY

June 2010

© Massachusetts Institute of Technology 2010. All rights reserved.

Author . . . .
Department of Mechanical Engineering
May 7, 2010

Certified by . . . .
Gang Chen
Carl Richard Soderberg Professor of Power Engineering
Thesis Supervisor

Accepted by . . . .
David E. Hardt
Chairman, Department Committee on Graduate Students

Experimental Investigations of Solid-Solid Thermal Interface Conductance

by

Kimberlee Chiyoko Collins

Submitted to the Department of Mechanical Engineering
on May 7, 2010, in partial fulfillment of the
requirements for the degree of
Master of Science in Mechanical Engineering

Abstract

Understanding thermal interface conductance is important for nanoscale systems where interfaces can play a critical role in heat transport. In this thesis, pump and probe transient thermoreflectance methods are used to measure the thermal interface conductance between solid materials. Two experimental studies of thermal interface conductance are presented, each revealing the complexity of phonon interactions at interfaces which are inadequately captured by current models of phonon transmissivity. The first study considers interfaces of different metals with graphite, and finds that atomic-scale roughness at the interface could be appreciably influencing the heat transport due to the extreme anisotropy of graphite. The thermal interface conductance of graphite is found to be similar to that of diamond, suggesting that when estimating the thermal interface conductance between metal and multi-walled carbon nanotubes (MWCNTs), a reasonable assumption may be that the conductance with the side walls of the MWCNTs is similar to the conductance with the ends of the MWCNTs. The second study considered aluminum on diamond interfaces where the diamond samples were functionalized to have different chemical surface terminations. The surface termination of the diamond is found to significantly influence the heat flow, with oxygenated diamond, which is hydrophilic, exhibiting four times higher thermal interface conductance than hydrogen-treated diamond, which is hydrophobic. Microstructure analysis determined that the Al film formed similarly, independent of diamond surface termination, suggesting that differences in interface bonding likely caused the observed difference in thermal interface conductance, a phenomenon which is not captured in current models of solid-solid phonon transmissivity.

Thesis Supervisor: Gang Chen
Title: Carl Richard Soderberg Professor of Power Engineering

Acknowledgments

This thesis owes its completion to the support of numerous individuals. My advisor, Prof. Gang Chen, provided me with the opportunity to work on exciting projects and offered me patient guidance and direction. Aaron Schmidt, built the pump and probe transient thermorefelctance (TTR) experiment in the Warren M. Rohsenow Heat and Mass Transfer Laboratory at MIT, and spent countless hours passing his knowledge along to me. Xiaoyuan Chen helped instruct me in optics and frequently contributed his expertise to troubleshooting difficulties. He and Aaron both reinforced my caution in working with class 4 laser systems. Austin Minnich frequently provided help with both experimental and theoretical challenges, and proved to be a valuable learning partner. Several individuals have frequently leant their optics expertise to us, including Darius Torchinsky, Jeremy Johnson, Christoph Klieber, and others in Prof. Keith Nelson's lab at MIT. Wilfredo Gonzalez from Spectra Physics offered prompt help with laser troubles. Microfabrication was done at the Microsystems Technology Laboratory at MIT, with notable help from Kurt Broderick and Dave Terry. Microscopy was done in the MIT Center for Materials Science and Engineering.

Several acknowledgments are specific to the studies presented in this thesis. Samples of highly ordered pyrolytic graphite (HOPG) and advice on the preparation of HOPG were provided by Prof. Mildred Dresselhaus, Xiaoting Jia, Alfonso Cecco and Daniel Nezich. Patrick Hopkins provided helpful discussions regarding the application of the diffuse mismatch model to anisotropic materials. Patrick Boisvert provided help with scanning electron microscope (SEM) imaging of graphite samples. Prof. Mildred Dresselhaus offered valuable input during the preparation of our graphite work for presentation at the 2009 Materials Research Society Fall meeting. Diamond samples were provided by Apollo Diamond, Inc. Patrick Doering offered instructive input on diamond and surface treatments. Elisabeth Shaw performed x-ray photo electron spectroscopy measurements on the diamond samples, Shuo Chen performed SEM and atomic force microscope imaging, and Shiahn Chen performed focused-ion-beam microscopy. Prof. Michael Rubner provided access to a goniometer.

I would like to thank my lab mates in the NanoEngineering group. I benefitted from many hours of discussions of both a technical and non-technical nature. Also, due to a major renovation of the Rohsenow Lab, the TTR system had to be moved to temporary space in the summer of 2009. This daunting task could not have been completed without the vigorous efforts of my lab mates Kenneth McEnaney, Daniel Kraemer and Maria Luckyanova, and without the constant support of Dick Fenner and Mark Ralph. Poetro Sambegoro and others in the NanoEngineering group also contributed significantly.

The support of many enabled me to attend MIT both as an undergraduate and as a graduate. Listed in the chronological order in which they impacted my path: Wes Masuda, Le Jardin Academy, Iolani School, Gerry Luppino, Prof. George Ricker, Joel Villasenor, MIT Lincoln Laboratory, John Sultana, Prof. John Heywood, Prof. Thomas Peacock, Prof. Carol Livermore, and all those who helped me to learn and to grow.

Finally, above all else, I thank my family and friends whose unwavering love carries me through all of life's adventures.

Contents

1 Introduction **15**

1.1 Background on Thermal Interface Conductance 15

1.1.1 Temperature Definition 19

1.1.2 Basic Theories of Phonon Transmissivity 21

1.1.3 Other Factors Influencing Thermal Interface Conductance 25

1.2 Organization of Thesis 27

2 Transient Thermoreflectance Experiment **29**

2.1 Background on Transient Thermoreflectance Measurements 29

2.1.1 Absorption of Laser Light in a Metal Film 31

2.2 Experimental System 35

2.2.1 Model for Data Analysis 38

2.2.2 Sample Preparation 41

2.2.3 Temperature Dependent TTR 44

2.3 Summary 45

3 Thermal Conductance at Metal-Graphite Interfaces **47**

3.1 Motivation and Background 47

3.2 Samples 48

3.3 Results 50

3.4 Modeling 53

3.5 Comparison to Diamond 57

3.6 Graphite Transmissivity 59
3.7 Summary 60

4 Effects of Surface Chemistry on Thermal Conductance at Al-Diamond Interfaces 63
4.1 Motivation and Background 63
4.2 Samples and Surface Characterization 65
4.3 Thermal Interface Conductance Results 67
4.3.1 Experimental Details 67
4.3.2 Results and Discussion 69
4.4 Investigations of Al Grain Structure 70
4.5 Summary 73

5 Conclusion 75
5.1 Summary 75
5.2 Future Work 77

List of Figures

1-1 Diagram of temperature discontinuity at an interface between two materials in intimate contact undergoing a heat flux. 16
1-2 Angle definitions for incident phonon. 17
1-3 Illustration comparing the temperature of phonons incident on an interface to the equivalent equilibrium temperature. 20
1-4 Specular vs diffuse phonon scattering assumptions of the AMM and DMM respectively. 22
1-5 Schematic diagram illustrating the path for heat flow across a metal-nonmetal interface. 27

2-1 Approximate film temperature rise due to a single laser pulse. 33
2-2 Approximate steady state film temperature rise. 35
2-3 TTR experimental setup diagram. 37
2-4 Diagram of layered sample. 40
2-5 Typical TTR signal for a sample of Al on Si. 43
2-6 Schematic of cryostat showing sample mounted to cold finger with a thin glass slide to collect condensation. 46

3-1 SEM images of HOPG samples coated in (a) Al, (b) Au, (c) Cr and (d) Ti. 49
3-2 Scaled room temperature thermoreflectance signals for various metals on HOPG. 50
3-3 Measured thermal interface conductance values for various metals on HOPG as a function of temperature. 51

3-4 Measured room temperature thermal interface conductance values for various metals on HOPG plotted as a function of the Debye temperature of the metal. 52

3-5 Measured thermal interface conductance data compared to DMM results assuming only contributions from c-axis phonon velocity on the graphite side. 55

3-6 Measured thermal interface conductance data compared to DMM results. Calculated results shown assuming only c-axis phonon velocities (c-axis model), and assuming an average of a-axis and c-axis phonon velocities (avg model) in the graphite. 56

3-7 Measured thermal interface conductance data compared to literature metal-on-diamond results. 57

3-8 DMM calculations for the thermal interface conductance between various metals and (a) c-axis HOPG, (b) a-axis HOPG, (c) diamond, and (d) HOPG with an average of a-axis and c-axis sound speeds. 58

3-9 Best fit curves of measured thermal interface conductance using a sine dispersion relation and allowing phonon transmissivity to vary. 60

4-1 Contact angle of DI water on (100) polished surfaces of (a) H-treated low purity, (b) H-treated medium purity, (c) oxygenated low purity, and (d) oxygenated medium purity single crystal diamond samples. . 66

4-2 Typical scaled TTR signals at room temperature for H-treated and oxygenated samples. 68

4-3 Measured thermal interface conductance between Al and H-treated low purity, H-treated medium purity, oxygenated low purity, and oxygenated medium purity single crystal diamond samples. 69

4-4 SEM images of Al film on (a) H-treated medium purity diamond and (b) oxygenated medium purity diamond. 71

4-5 AFM images of Al film on (a) H-treated medium purity diamond and (b) oxygenated medium purity diamond. 71

4-6 FIB microscopy images of Al film grain structure at the interface with (a) H-treated medium purity diamond and (b) oxygenated medium purity diamond. 72

List of Tables

2.1 Optical absorption depths for various metals at wavelengths of 400 *nm* and 800 *nm*. 42

3.1 Electron-phonon coupling constants and phonon thermal conductivities in Al and Au. 55

3.2 Comparison of room temperature calculated thermal interface conductance accounting for electron-phonon coupling in the metal to the DMM, which only accounts for phonon-phonon coupling at the interface.. 56

3.3 Phonon transmissivities at metal-graphtie interfaces. 60

4.1 XPS measured atomic concentrations within the first few atomic layers of the sample surfaces. 66

Chapter 1

Introduction

The study of solid-solid thermal interface conductance has wide-ranging applications in nanoscale systems, where interfaces can play a critical role in heat transfer. As the length scale for conduction is reduced, the small values of thermal interface resistance (typically on the order of $1\times10^{-8}m^2K/W$) can be on the same order or greater than other conduction resistances in the system. Thermal interface conductance has been studied for over half a century, but the field still lacks a comprehensive understanding of all the mechanisms which contribute to interfacial heat transport [1, 2].

1.1 Background on Thermal Interface Conductance

Thermal interface resistance is a measure of the resistance to heat flow at the interface between two materials in intimate contact. The term,"intimate contact" indicates that no microscale voids exist at the interface, which provides an important distinction with other work studying the effects of imperfect contact on heat flow [3]. Even in the limit of perfect contact, a temperature discontinuity exists at the interface between materials undergoing a heat flux as diagramed in Fig. 1-1.

The terms "thermal interface conductance" and "thermal interface resistance" are used interchangeably to describe the same temperature discontinuity, with conductance simply representing the inverse of resistance. The physical origin of thermal interface resistance stems from the response of energy carriers, primarily phonons,

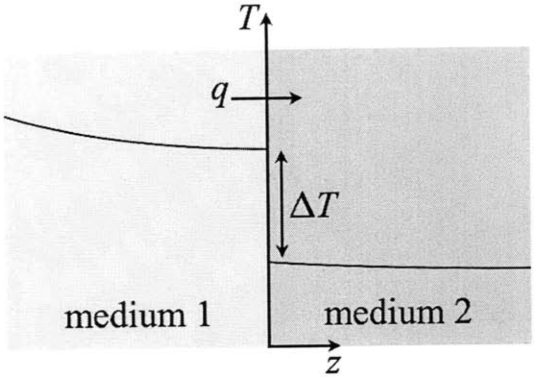

Figure 1-1: Schematic diagram showing temperature discontinuity, ΔT, at the interface between two materials in intimate contact undergoing a heat flux, q. The cross-plane direction is designated as the z direction.

incident on an interface. Phonons are quantized lattice vibrations that transmit heat and sound in a material. When a phonon is incident on an interface, it has a certain probability of transmitting across that interface. This finite phonon transmissivity gives rise to a temperature discontinuity.

Some of the earliest interest in thermal interface resistance stemmed from work in cryogenic science, and efforts to achieve temperatures below a few millikelvin [4]. The first experimental observation was reported by Kapitza in 1941, who found that a finite temperature discontinuity existed at the interface between liquid He and a solid [5]. Later work found similar temperature discontinuities at solid-solid boundaries [2]. The focus of this thesis is on solid-solid boundaries in the temperature range from 80 K to 300 K.

For simplicity, the thermal interface conductance, G, can be described as the ratio between the net heat flux per unit area, q, across an interface to the temperature discontinuity, ΔT_e, at the interface as shown in Eq. (1.1), and has units of W/m^2K. An important subtlety exists, however, in the definition of temperature. The temperature on one side of an interface is taken to be the temperature corresponding to the distribution of phonons incident on the interface from that side [1], and this subtlety is indicated by the subscript e. Subscripts 1 and 2 describe the mediums on each side of the interface. The net heat flux, q, is the difference between the gross heat flux going from side 1 to side 2 and the gross heat flux returning from side 2 back to side 1.

$$G = \frac{q}{\Delta T_e} = \frac{q_{1\to2} - q_{2\to1}}{T_{e1} - T_{e2}} \tag{1.1}$$

The gross heat flux from medium 1 to medium 2, $q_{1\to2}$, can be expressed as the product of the phonon velocity normal to the interface, $v\cos\theta$, phonon energy, $\hbar\omega$, density of states, D, the Bose-Einstein distribution, f, and phonon transmissivity from medium 1 to medium 2, $\alpha_{1\to2}$, integrated over all phonon frequencies, ω, and solid angles, and summed over all phonon modes, j.

$$q_{1\to2} = \sum_j \frac{1}{4\pi} \int_0^{2\pi} d\phi_1 \int_0^{\pi/2} \sin\theta_1 d\theta_1 \int_0^{\omega_1^{max}} v_1 \cos\theta_1 \hbar\omega D_1(\omega) f(\omega, T_{e1}) \alpha_{1\to2}(\omega, \phi_1, \theta_1) d\omega \tag{1.2}$$

Here ϕ is azimuthal angle and θ is the angle between the wave vector of the incident phonon and the normal to the interface as illustrated in Fig. 1-2. Often, ω_1^{max} is taken to be the lower of the Debye frequency in either material.

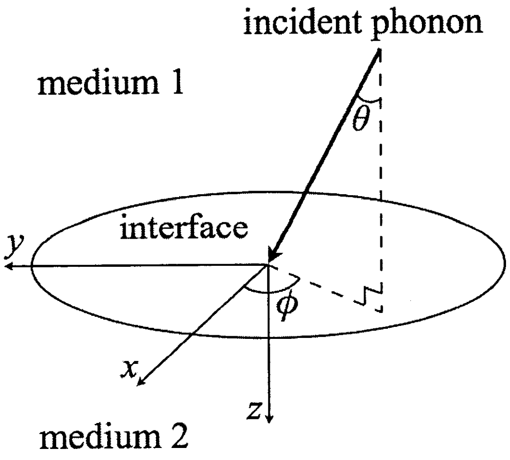

Figure 1-2: Angle definitions for incident phonon.

A similar expression may be written for $q_{2\to1}$. The net heat flux, q is the difference between $q_{1\to2}$ and $q_{2\to1}$. Using the principle of detailed balance, q can be written in terms of the properties in only one of the two mediums as shown in Eq. (1.3). The principle of detailed balance implies that in thermal equilibrium (when $T_{e1} = T_{e2}$), phonons of a given state leaving one side must be balanced by phonons returning from the other side into that same state such that the net heat flux is zero ($q = 0$).

$$q = \sum_j \frac{1}{4\pi} \int_0^{2\pi} d\phi_1 \int_0^{\pi/2} \sin\theta_1 d\theta_1 \int_0^{\omega_1^{max}} v_1 \cos\theta_1 \hbar\omega D_1(\omega)(f(\omega, T_{e1}) - f(\omega, T_{e2}))\alpha_{1\to2}(\omega, \phi_1, \theta_1) d\omega \tag{1.3}$$

By combining Eqs. (1.1) and (1.3), and taking the limit of small $T_{e1} - T_{e2}$, a general expression for G can be written.

$$G = \sum_j \frac{1}{4\pi} \int_0^{2\pi} d\phi_1 \int_0^{\pi/2} \sin\theta_1 d\theta_1 \int_0^{\omega_1^{max}} v_1 \cos\theta_1 \hbar\omega D_1(\omega) \frac{df(\omega, T_e)}{dT_e} \alpha_{1\to2}(\omega, \phi_1, \theta_1) d\omega \tag{1.4}$$

If the phonon transmissivity, $\alpha_{1\to2}$, can be taken to be independent of azimuthal angle, ϕ_1, which is true for isotropic mediums, the integration over ϕ_1 can be easily evaluated, simplifying the expression for G.

$$G = \sum_j \frac{1}{2} \int_0^{\pi/2} \sin\theta_1 d\theta_1 \int_0^{\omega_1^{max}} v_1 \cos\theta \hbar\omega D_1(\omega) \frac{df(\omega, T_e)}{dT_e} \alpha_{1\to2}(\omega, \theta_1) d\omega \tag{1.5}$$

Further simplifications to the expression for G can be made by recognizing that the product $\hbar\omega D_1(\omega) df/dT_e$ is the mode specific heat, $C_1(\omega)$, and by using the directional cosine, $\mu = \cos(\theta)$.

$$G = \sum_j \frac{1}{2} \int_0^1 \int_0^{\omega_1^{max}} v_1 C_1(\omega) \alpha_{1\to2}(\omega, \mu_1) d\omega \mu_1 d\mu_1 \tag{1.6}$$

Equations (1.5) and (1.6) are identical, but Eq. (1.6) treats G in the useful framework of mode specific heat. In the limit of low temperatures, when $\alpha_{1\to2}$ is independent of ω, these expressions give a T^{-3} temperature dependence for the interface resistance due to the T^3 temperature dependence of the specific heat, consistent with the observations of Kapitza. In principle, G can be calculated directly from the above expressions for any temperature range if the phonon transmissivity, $\alpha_{1\to2}$, is known. Equation (1.4) is most general, but the more simple expressions in Eqs. (1.5) and (1.6) frequently apply. Section 1.1.2 discusses the difficulties involved in modeling phonon transmissivity as well as the prevailing models in the literature.

1.1.1 Temperature Definition

Before concluding the discussion of thermal interface conductance, as modeled by Eq. (1.4), further discussion of the definition of temperature is required. One discrepancy in Eq. (1.4) is that it approaches a non-physical limit. In the case of imaginary interfaces, the thermal interface resistance should go to zero, and the phonon transmissivity should be unity. Taking $\alpha_{1\to2} = 1$ in Eq. (1.4), however, produces a non-zero interface resistance [2].

The origin of this non-physical result stems from the definition of temperature used. The temperature on one side of an interface has been taken to be the temperature of the phonons incident on that interface, denoted here by T_e. However, the definition of temperature on small length scales is not straight forward because the mean free paths of energy carriers is on the same order as the length scale over which a definition of temperature is attempted [6]. On either side of an interface, there are phonons incident on the interface at the temperature of their originating medium, as well as phonons reflected at the interface with a temperature determined by the original medium temperature and the reflectivity, in addition to phonons transmitted into the medium from the other side which have temperatures determined by the temperature of the other medium and the transmissivity. This range of energy carriers with different temperatures is depicted in Fig. 1-3a adapted from Ref. [6]. The local energy spectrum of phonons near an interface is different from the energy of the incoming phonons [7].

At high temperatures, heat is primarily carried by shorter wavelength phonons, making the physical measurement of T_e impractical, and a measurement of an equiv-

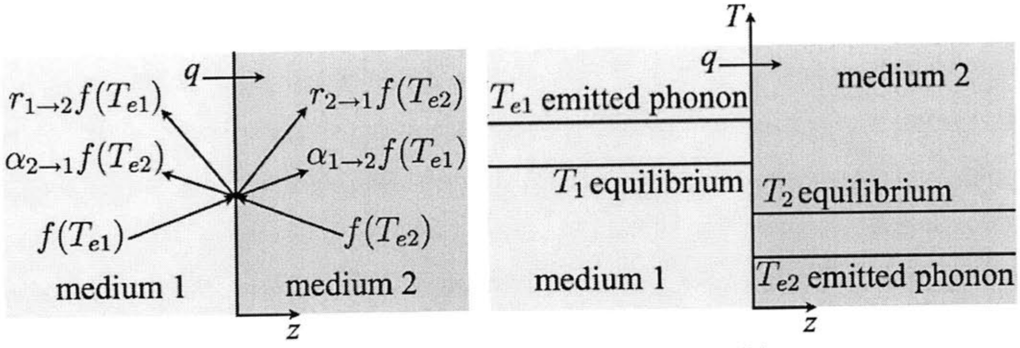
q
$r_{1\to2}f(T_{e1})$
$\alpha_{2\to1}f(T_{e2})$
$f(T_{e1})$
$r_{2\to1}f(T_{e2})$
$\alpha_{1\to2}f(T_{e1})$
$f(T_{e2})$
medium 1
medium 2
z
T
q
T_{e1} emitted phonon
medium 2
T_1 equilibrium
T_2 equilibrium
medium 1
T_{e2} emitted phonon
z

(a) (b)

Figure 1-3: (a)Schematic diagram of phonons at an interface and their corresponding range of temperatures. (b)Comparison of incident phonon temperature, T_e, and equivalent equilibrium temperature, T. Figure adapted from Ref. [6]

alent equilibrium temperature more likely. Here, T will be used to denote the equivalent equilibrium temperature. To relate T to T_e, we imagine that phonons at the interface adiabatically approach an equilibrium temperature, calling this temperature T, which is a representation of the local energy density. T is related to T_e as shown in Eqs. (1.7) and (1.8) [6]. This relationship assumes that $\alpha_{1\to2}$ is independent of ϕ.

$$T_1 = T_{e1} - \frac{(T_{e1} - T_{e2})}{2} \int_0^1 \alpha_{1\to2}(\mu_1) d\mu_1 \qquad (1.7)$$

$$T_2 = T_{e2} - \frac{(T_{e2} - T_{e1})}{2} \int_0^1 \alpha_{2\to1}(\mu_2) d\mu_2 \qquad (1.8)$$

Consequently, $\Delta T_{1\to2}$ becomes

$$\Delta T_{1\to2} = T_1 - T_2 = \Big[1 - \frac{1}{2}\Big\langle \int_0^1 \alpha_{1\to2}(\mu_1) d\mu_1 + \int_0^1 \alpha_{2\to1}(\mu_2) d\mu_2 \Big\rangle\Big](T_{e1} - T_{e2}) \qquad (1.9)$$

And based on Eq. (1.6), where the transmissivity is assumed independent of ϕ, the thermal interface conductance defined in terms of local energy density becomes

$$G = \frac{q}{T_1 - T_2} = \sum_j \frac{\frac{1}{2}\int_0^1 \int_0^{\omega_1^{max}} v_1 C_1(\omega)\alpha_{1\to 2}(\omega, \mu_1) d\omega \mu_1 d\mu_1}{\left[1 - \frac{1}{2}\left\langle \int_0^1 \alpha_{1\to 2}(\omega, \mu_1) d\mu_1 + \int_0^1 \alpha_{2\to 1}(\omega, \mu_2) d\mu_2 \right\rangle\right]} \tag{1.10}$$

This expression has the correct limit that when $\alpha_{1\to 2} = 1$ and $\alpha_{2\to 1} = 1$, the thermal boundary resistance goes to zero. This correction to the model for thermal interface conductance was proposed by Chen and Zeng in 2001 [6]. Katerberg also considered the effect of temperature definition on the calculations of thermal boundary resistance, and pointed out that the correct model to use depends on the specifics of the experiment [7]. At low temperatures, it is possible to carefully design an experiment to measure incident phonon temperature, T_e, making Eq. (1.4) a valid definition [1]. At higher temperatures, however, most experiments are only able to measure a local temperature that is better approximated by T, and Eq. (1.10) should be used.

1.1.2 Basic Theories of Phonon Transmissivity

The challenge in modeling thermal interface conductance is primarily one of modeling phonon transmissivity. The behavior of energy carriers incident on an interface is rather complex. For example, a phonon incident on an interface might transmit or reflect, it could mode convert, or scatter into a different energy state, or even couple to electrons. The transmission probability for a phonon can depend on its frequency, mode, angle of incidence, the density of phonon states in the materials, temperature in the event of anharmonic interactions, and the physical condition of the interface.

Two primary models for thermal interface conductance exist in the literature, and each assumes a different limit for phonon scattering. The acoustic mismatch model (AMM) assumes that all phonons reflect specularly with no scattering at an interface, while the diffuse mismatch model (DMM) assumes that all phonons scatter diffusely, as illustrated in Fig. 1-4. Each of these models will be discussed in further detail.

The AMM was the earliest model used to explain the resistance at the interface between solids and liquid He. It was first proposed by Khalatnikov in 1952 [8]. In

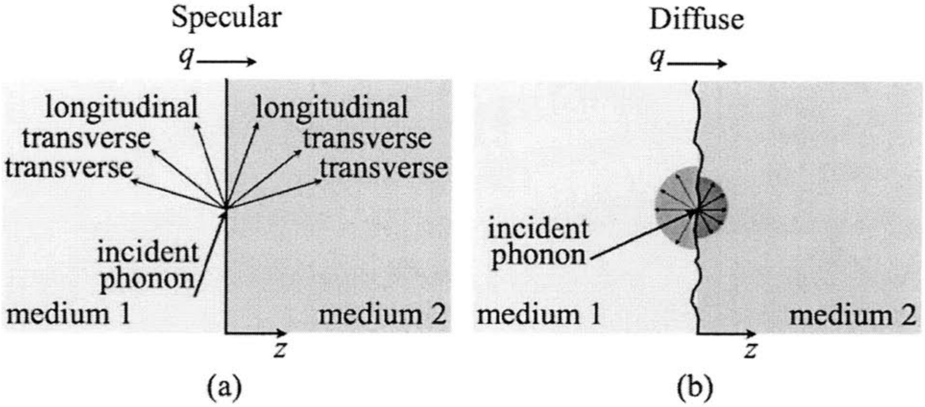
Specular
q
longitudinal
transverse
transverse
longitudinal
transverse
transverse
incident
phonon
medium 1
medium 2
z
(a)
Diffuse
q
incident
phonon
medium 1
medium 2
z
(b)

Figure 1-4: Schematic diagram illustrating the response of phonons at an interface according to (a) the AMM which assumes specular scattering and (b) the DMM which assumes diffuse scattering.

1959, Little extended the AMM to apply for solid-solid boundaries [2]. The AMM models the interface as a flat plane and phonons as obeying continuum acoustics, whereby phonons reflect and refract with and without mode conversion. Acoustic impedances in the materials determine the degree of phonon reflection and refraction, where acoustic impedance, Z, is defined as the product of mass density, ρ, and phonon veolcity, v.

$$Z = \rho v \tag{1.11}$$

The angles of phonon reflection and refraction are determined by the acoustic equivalent of Snell's Law. For shear waves, a simple expression can be written, where θ_1 is the angle of the incident phonon wave vector to the interface normal, θ_2 is the refracted angle, and the phonon is taken to be going from medium 1 to medium 2.

$$\frac{\sin\theta_1}{\sin\theta 2} = \frac{v_1}{v_2} \tag{1.12}$$

In the simple case of a transverse acoustic wave polarized perpendicular to the plane of incidence, the AMM gives the transmissivity expression shown in Eq. (1.13), where μ is the directional cosine ($\mu_1 = \cos(\theta_1)$ and $\mu_2 = \cos(\theta_2)$).

$$\alpha_{1\to2}(\mu_1) = \frac{4Z_1Z_2\mu_1\mu_2}{(Z_1\mu_1 + Z_2\mu_2)^2} \tag{1.13}$$

Using the AMM for transmissivity, a T_e^{-3} temperature dependence is predicted for the thermal interface resistance, consistent with the observations of Kapitza [5], but its accuracy in matching experimental results is limited by the assumption of specular phonon reflection. Small-scale imperfections at an interface cause high frequency phonons to scatter. Low temperatures help to mitigate the likelihood of phonon scattering because at low temperatures, longer wavelength phonons are the dominant energy carriers. Consequently, the AMM works best for very clean, defect-free interfaces at low temperatures, and surface preparation is critical [1].

The DMM, introduced by Swartz in 1987, assumes that all phonons "forget" where they came from and what modes they had when encountering an interface, and scatter both diffusely and elastically [1, 9]. Thus, the transmission probability depends only on the phonon density of states on both sides of the interface, while satisfying the principle of detailed balance. The assumption of the DMM implies that the phonon reflectivity from medium 1 to medium 2 equals the transmissivity from medium 2 to medium 1, as shown in Eq. (1.14). On the left hand side, conservation of energy has been employed to write the reflectivity in terms of the transmissivity, using the relation that reflectivity plus transmissivity must equal unity.

$$1 - \alpha_{1\to2} = \alpha_{2\to1} \tag{1.14}$$

Combining Eq. (1.14) with the principle of detailed balance, an expression for $\alpha_{1\to2}$ can be obtained. In the limit of low temperatures, a linear Debye approximation for the phonon dispersion relation may be used, which leads to the following transmissivity expression [1]. Here all phonon polarizations are being lumped together into a single average phonon velocity in the medium.

$$\alpha_{1\to2} = \frac{1/v_2^2}{1/v_1^2 + 1/v_2^2} \tag{1.15}$$

At higher temperatures, the linear approximation breaks down, and a more realistic phonon dispersion is needed [10, 11]. Dames and Chen found a more general expression for $\alpha_{1\to2}$, shown in Eq. (1.16), that applies to both low and high temperatures [12].

$$\alpha_{1\to2} = \frac{v_2 U_2(T_e)}{v_1 U_1(T_e) + v_2 U_2(T_e)} \tag{1.16}$$

where $U(T_e)$ is the volumetric internal energy,

$$U = \int_0^{T_e} C(T)dT \tag{1.17}$$

Written in terms of frequency instead of temperature, an equivalent expression to Eq. (1.16) for $\alpha_{1\to2}$ is

$$\alpha_{1\to2} = \frac{\int_0^{\omega^{max}} v_2 \hbar\omega D_2 f d\omega}{\int_0^{\omega^{max}} v_1 \hbar\omega D_1 f d\omega + \int_0^{\omega^{max}} v_2 \hbar\omega D_2 f d\omega} \tag{1.18}$$

Both Eqns. (1.15) and (1.16), however, have the flaw that they predict that the phonon transmissivity approaches 1/2 in the limit of an imaginary interface. As discussed in Sec. 1.1.1, in the limit of an imaginary interface, the transmissivity should approach unity. The DMM has mixed success matching experimental results. The next section discusses efforts to go beyond the assumptions of the DMM and account for other factors that could influence interfacial heat transport.

Before going further, it is worth mentioning the limiting model for phonon transmissivity. The so called "perfect match model" or phonon radiation limit sets the upper limit for thermal boundary conductance assuming purely elastic scattering events [13]. The model asserts that the maximum thermal interface conductance is achieved when all phonons from the side with the lower population density of phonons transmit across the interface. Under the assumption of purely elastic scattering, this is an upper limit because it represents the maximum number of phonons which can transmit across the interface while satisfying the principle of detailed balance. Stoner and Maris derived the following expression for the phonon radiation limit of the thermal interface conductance, G_{rad}, assuming isotropic mediums and purely elastic scattering events, where ω_{max} is taken as the lower of the two Debye frequencies and c_D is the Debye velocity of the other medium [14]. The Debye velocity c_D is a function of the average longitudinal, c_l, and transverse, c_t, sound velocities in the material.

$$G_{rad} = \frac{1}{16\pi^2}\frac{3}{c_D^2}\int_0^{\omega_{max}} \frac{df(\omega,T_e)}{dT}\hbar\omega^3 d\omega \tag{1.19}$$

$$\frac{3}{c_D^2} = \frac{1}{c_l^2} + \frac{2}{c_t^2} \tag{1.20}$$

In the limit of high temperatures, this becomes [15]

$$G_{rad} = \frac{k_B\omega_{max}^3}{8\pi^2 c_D^2} \tag{1.21}$$

For instance, consider an interface with aluminum on one side and diamond on the other. Since aluminum has the lower Debye frequency of the two materials, all phonons in the diamond with a frequency less than the Debye frequency of aluminum will transmit across the interface, and no phonons in diamond with higher frequencies will transmit, unless inelastic scattering occurs. Thus, the phonon radiation limit would be calculated by taking c_D of diamond and ω_{max} of aluminum. If the measured thermal interface conductance exceeds the phonon radiation limit, then inelastic phonon scattering at the interface must be significant [14].

1.1.3 Other Factors Influencing Thermal Interface Conductance

The models of thermal interface conductance discussed thus far have limited success in matching experimental results [1, 16]. Other heat transport mechanisms that go beyond the assumptions of the AMM and the DMM have been explored in the literature [14, 17, 18, 19, 20]. Here we mention a select few of these efforts.

The contribution of inelastic scattering at interfaces between metals and dielectrics that have highly mismatched Debye temperatures was found to be significant, since the measured thermal interface conductance was higher than the calculated phonon radiation limit [14, 18]. Specifically, Pb-diamond, Pb-sapphire and Au-diamond [14], and Bi-diamond [15], interfaces were found to have higher conductances than predicted by the phonon radiation limit, suggesting inharmonic scattering processes. The contribution of inelastic scattering has been found to increase with increasing interfacial acoustic mismatch [18]. In the Pb-diamond system, it was also found that anharmonic processes could explain the high measured values of conductance [14].

Majumdar and Reddy have considered the effect of electrons in the metal film influencing the thermal interface conductance at metal-nonmetal interfaces [20], following the approach of Yoo and Anderson who developed a similar analysis for thermal interface conductance between superconductors and dielectrics [21]. Using a simple two temperature model in the metal [22], and neglecting coupling of electrons in the metal to phonons in the nonmetal, they derived an expression for thermal interface conductance that accounted for both the resistance of electron-phonon energy transfer in the metal, R_{ep}, and the resistance of phonon-phonon energy transfer at the metal-nonmetal interface, R_{pp}, as illustrated in Fig. 1-5. Their approximate expression for thermal interface conductance, h, is shown in Eq. (1.22), where h_{ep} and h_{pp} are respectively the electron-phonon conductance in the metal and the phonon-phonon conductance at the interface. The phonon-phonon conductance at the interface is calculated using the DMM. The electron-phonon conductance in the metal is defined in terms of the electron-phonon coupling constant in the metal, $G_{coupling}$, and the phonon contribution to the thermal conductivity in the metal, k_p. Their model had success in lowering the over-prediction of the DMM in the case of the highly acoustically matched interface between epitaxial TiN and MgO [20, 23].

$$h \approx \frac{h_{ep} h_{pp}}{h_{ep} + h_{pp}} \tag{1.22}$$

$$h_{ep} = \sqrt{G_{coupling} k_p} \tag{1.23}$$

The effect of atomic mixing at interfaces has been investigated for interfaces of

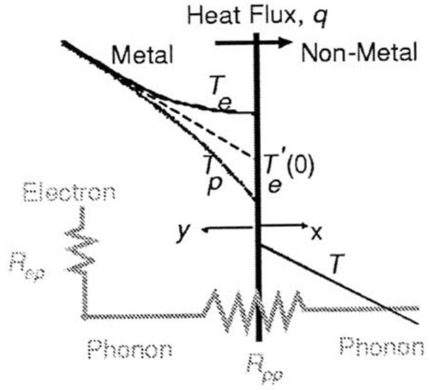

Figure 1-5: Schematic diagram illustrating the path for heat flow across a metal-nonmetal interface. Figure reproduced from Ref. [20]

Cr on Si [17, 24]. It was found the the virtual crystal DMM could explain the experimental findings based on the thickness of the mixed, two-phase region.

Prasher extended the AMM to account for the strength of interfacial bonding [19]. He found that for weak bonding such as van der Waals interactions, adhesion energy is proportional to the conductance per unit area and should be accounted for in the calculation of thermal interface conductance. For strong bonding, the model predictions matched the traditional AMM.

Here we have mentioned a select few examples of analytical efforts to improve upon the traditional AMM and DMM. Further experimental and theoretical work, however, is needed to develop a complete understanding of the complex phenomenon of thermal interface conductance.

1.2 Organization of Thesis

Experimental investigations of thermal interface conductance can contribute to understanding this complex phenomenon. Several careful experiments that each revel complex processes affecting thermal interface conductance will be presented in this thesis. The scope of these experimental studies is limited to interfaces between solid materials in the temperature range from 80 K to 300 K. Chapter 1 discussed background information on thermal interface conductance theory. Chapter 2 presents the details of our experimental system. Chapter 3 presents a study of thermal interface conductance in metal-on-graphite systems, where the anisotropy of the graphite in conjunction with atomic scale roughness is thought to have influenced the interfacial heat transport. Chapter 4 covers a study of thermal interface conductance at aluminum-diamond interfaces, where it is found that the surface chemistry of the diamond has a strong influence on the interfacial heat conduction. Finally, Chapter 5 summarizes our findings and discusses planned future work.

Chapter 2

Transient Thermoreflectance Experiment

2.1 Background on Transient Thermoreflectance Measurements

Pump and probe transient thermorefelctance (TTR) experiments are able to measure the thermal properties of samples by heating the surface with a pulsed laser, and subsequently measuring the change in surface temperature optically [16, 25, 26, 27, 28]. The system utilizes small changes in the surface reflectivity due to thermal excitation to measure the temperature change at the surface as a function of time, and from that, infer thermal property data. The arrival of the pulsed heating (pump) and measuring (probe) beams are separated by an adjustable delay that allows for time resolved measurements of surface cooling. The time resolution of the measurement is typically limited by the width of the pump pulse (200 fs for our system). Thus, the measurement has subpicosecond time resolution, which allows for the study of transient heat transfer processes. TTR is a non-contact, non-distructive method for measuring thermal properties. It is especially useful for measuring interfaces and thin films, for which traditional thermal property measurements are impractical due to contact resistance issues.

The first TTR system was built by Paddock and Eesley in 1986 [25]. They used a mode-locked argon-ion laser to synchronously pump two ring dye lasers. One dye laser served as the pump with a wavelength of 633 *nm* and a pulse width of 8 *ps*, and the other served as the probe with a wavelength of 595 *nm* and a pulse width of 6 *ps*. Both pump and probe had repetition rates of 246 MHz, or 4 *ns* between pulses. The major elements used by Paddock and Eesley are still those used in TTR systems: a mechanical delay stage to time delay the probe relative to the pump, a modulator to chop the pump beam at a reference frequency, and a lock-in amplifier to detect the signal from the small changes in reflectance at the surface (10^{-4}).

In 1996, Capinski and Maris made several notable improvements to the TTR system design [26]. The mechanical delay stage used to time delay the probe relative to the pump introduced significant alignment challenges. For accurate interpretation of measured TTR data, maintaining complete overlap of the pump and probe beams on the sample surface at every time step is critical. The introduction of huge (several meters) spatial path length variations in the probe beam made the alignment of pump and probe on the sample a significant source of error, and limited the reliable time-resolved data in TTR measurements to a few hundreds of picoseconds. To mediate this difficulty, Capinski and Maris used an optical fiber to deliver the probe pulse from the delay stage to the sample. This change produced a probe spot on the sample of a fixed size and location regardless of the delay stage position, allowing reliable measurements of time-resolved data out to the full length of the delay stage. Their TTR system consisted of a single dye laser with a wavelength of 632 *nm*, that output pulses 200 fs wide at a repetition rate of 76 MHz. The shorter pulse width gave their measurement subpicosecond resolution.

Cahill and coworkers made further improvements to TTR experimental ease-of-use and accuracy [16, 27, 28]. By adding an inductive resonator between the photodiode detector and the lock-in amplifier, they improved signal-to-noise by a factor of 10 or more. The pump modulation frequency is chosen to match the resonator frequency, allowing the resonator to amplify the signal of interest. Cahill also incorporated RF chokes on long electrical wires to reduce noise from coherent radio frequencies. To simplify the process of placing the sample surface at a consistent focal plane, a charged coupled device (CCD) camera was introduced, effectively creating a microscope integrated into the TTR system. Accessed through a removable mirror, the CCD camera provided great benefits, not only for focusing, but also for selecting measurement locations on the sample. Cahill's TTR system uses a Ti:sapphire oscillator, which outputs 150 fs long pulses at a repetition rate of 80 MHz and a wavelength of 790 nm. The TTR system we use, described in Sec. 2.2 borrows many of Cahill's innovations, and adds a few new improvements [28].

2.1.1 Absorption of Laser Light in a Metal Film

Typically in transient thermorefelctance experiments, samples are coated in a thin metal film. The film acts to absorb the pump laser light, and its reflectance changes as a function of temperature. Short pulses of pump light heat the metal film by exciting electrons near the surface to higher energy states [29, 30, 31, 32]. These hot electrons can reach temperatures of several thousand degrees Kelvin due to the small values of electronic heat capacity [33], and rapidly diffuse throughout the metal film. Hot electrons can uniformly distribute throughout a 100 to 300 nm thick metal film in 100 to 300 fs [34]. The electrons then thermalize, exciting phonons in the metal. These phonons then traverse the interface, exciting phonons in the underlying substrate. It is worth noting that for electrically conducting substrates, it is also possible for electrons in the metal to couple to phonons or to electrons in the underlying substrate.

The reflectivity of the metal film is a function of the film temperature because temperature affects the occupation probability of electrons [29, 30]. As electrons are excited to higher energy states, the probability of further excitation decreases, thus decreasing the photon absorption and increasing the reflectivity. The change in reflectivity due to pulsed laser heating in TTR experiments if very small, on the order of 10^{-4}, and thus lock-in detection is required.

In 1974, Anisimov introduced a two temperature model to describe the interaction of electrons and phonons in a metal film [35]. Electrons and phonons are thought of as having different and distinct temperatures, T_e and T_p, and their energy transfer rate is taken to be proportional to an electron-phonon coupling constant, $G_{coupling}$. This model makes it possible to estimate the time it takes for electrons and phonons in the metal to reach local thermal equilibrium. The equilibrium time constant is given by Eq. (2.1), where C_e and C_p are respectively the electron and phonon volumetric heat capacities. Accurately calculating the time constant from this formulation, however, is challenging because the heat capacity of the hot electrons is not well known. Nevertheless, approximate values of heat capacity give an equilibration time of approximately 1 to 100 ps [28].

$$\tau = \frac{1}{G_{coupling}(C_e^{-1} + C_p^{-1})} \tag{2.1}$$

The time constant for temperature inside Al film to become uniform, whereby electrons have homogenized the film temperature, can be approximated as the time constant for diffusion in an insulated film as shown in Eq. (2.2), where d is the thickness of the metal film and α is the thermal diffusivity of the metal film [36]. For a 100 nm thick film of Al with a thermal diffusivity of 0.97 cm^2/s, at room temperature, τ is about 10.5 ps. At 80 K, when the thermal diffusivity of the Al film is 3.44 cm^2/s, τ is about 3 ps. Even if the thermal diffusivity in the Al film were much less than the bulk value, say by a factor of two, the time constant would still be on the order of tens of picoseconds: 21 ps at room temperature and 6 ps at 80 K.

$$\tau \approx \frac{d^2}{\pi^2 \alpha} \tag{2.2}$$

Both methods imply that the thin metal film will have a uniform, well defined temperature within a few tens of picoseconds. After a uniform temperature has been established, the heat transport through the sample may be modeled using Fourier's law of heat conduction, as discussed in Section 2.2.1.

The increase in film temperature resulting from a singe laser pulse may be estimated from Eq.(2.3), where R is the reflectivity of the metal film, Q is the energy of the laser pulse, C is the volumetric specific heat of the metal film, and A is the area of the laser spot [36]. The reflectivity of Al at 400 nm is approximately 0.92 and at 800 *nm* is approximately 0.87 [37]. Figure 2-1 shows the calculated temperature rise of a 100 *nm* thick Al film. Calculations are shown for two different laser beams, a pump beam and a probe beam. The wavelength and power values used for the pump and probe beams is representative of our experimental system, which will be discussed in Section 2.2. Generally, our probe beam diameter is 10 μm and our pump beam diameter is 40 to 100 μm, resulting in a temperature rise of less than 1.5 K at room temperature and less than 4 K at a sample temperature of 80 K. These small temperature rises allow us to approximate that the thermoreflectance coefficient is linearly proportional to temperature [38].

$$\Delta T = \frac{(1-R)Q}{CAd} \tag{2.3}$$

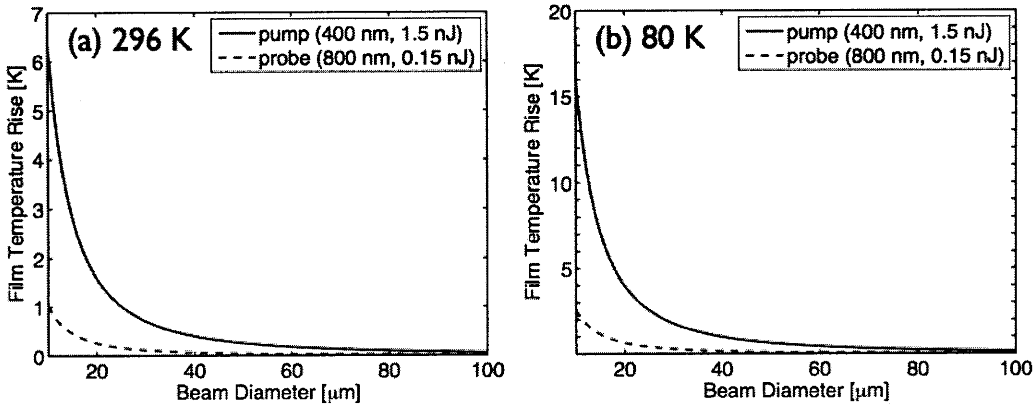

Figure 2-1: Approximate temperature rise in a 100 *nm* thick Al film resulting from a single laser pulse as a function of laser spot diameter for a sample at (a) 296 K and (b) 80 K. Values shown for two different laser pulses: a 400 *nm* pump pulse with 1.5 nJ of energy per pulse and a 800 *nm* probe pulse with 0.15 nJ of energy per pulse.

While the single pulse film temperature rise is an important parameter for validating the assumption of a linear relationship between film temperature and thermoreflectance coefficient, the heating due to multiple pulses must also be considered. An expression for the steady state temperature rise of the surface may be derived by assuming the low frequency limit of periodic heating at the surface [39]. Physically in TTR experiments, the surface is heated by a series of delta function heat inputs. The envelope of the heat inputs, however, is that of a sinusoid, so a reasonable upper limit for the steady state heating may be derived by considering a periodic heat input, which greatly simplifies the solution. Cahill derived this solution by assuming a periodic point source heating of the surface, and accounting for the gaussian intensity distributions of the pump and probe beams [39]. Equation (2.4) shows the resulting surface temperature rise, where the frequency response, $H(\omega)$, is given by Eq. (2.5). Here, A is the amplitude of the absorbed laser power, w_0 and w_1 are the $1/e^2$ radii of the pump and probe beams respectively, k is the thermal conductivity of the surface layer, α is the thermal diffusivity of the surface layer, and ω is the frequency of the periodic heat input.

$$\Delta T = 2\pi A \int_0^\infty H(n) exp(-\pi^2 n^2 (w_0^2 + w_1^2)/2) n dn \tag{2.4}$$

$$H(\omega) = \frac{1}{k(4\pi^2 n^2 + i\omega/\alpha)^{1/2}} \tag{2.5}$$

In the limit of low frequencies, Eq. (2.4) may be simplified to Eq. (2.6), which gives the steady state surface temperature rise due to heating by the pump and probe beams, and which is plotted in Fig. 2-2. The surface layer is assumed to be aluminum, with a thermal conductivity of 237 W/mK at room temperature, and a thermal conductivity of 333 W/mK at 80 K. The amplitude of the heat absorbed is estimated to be 10 mW because the reflectivity of Al at 400 nm is approximately 90 percent and the power of the pump light incident on the surface during our experiments is approximately 100 mW. The probe $1/e^2$ radius is held constant at 5 μm, which is typical in our experiments, and the pump $1/e^2$ radius is allowed to vary from 5 μm to 50 μm. The calculation shows that the steady state temperature rise of the surface due to laser heating is generally less than 2 K.

$$\Delta T = \frac{A}{k}\sqrt{\frac{1}{2\pi(w_0^2 + w_1^2)}} \tag{2.6}$$

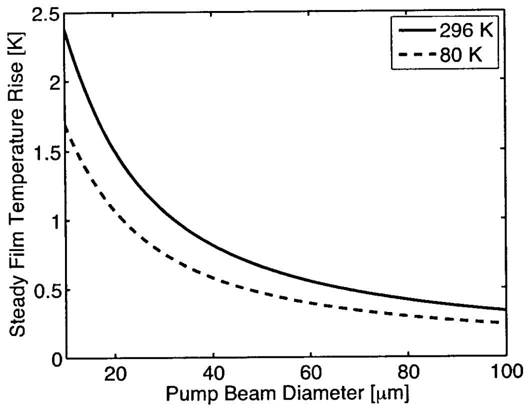

Figure 2-2: Approximate steady state temperature rise of an Al film as a function of pump beam diameter. The diameter of the probe beam is assumed constant at 10 μm. Curves are shown for sample temperatures of 80 K and 296 K.

2.2 Experimental System

The pump and probe transient thermoreflectance system in the Warren M. Rohsenow Heat and Mass Transfer Laboratory at MIT was constructed by Aaron J. Schmidt as part of his Ph.D. work in the Department of Mechanical Engineering. Here, we highlight merely a few of the key aspects pertaining to the TTR system, and refer the reader to Schmidt's Ph.D. thesis for a comprehensive description of both the system and the thermal modeling [28].

Figure 2-3, adapted from [28], diagrams all the major optical components of our experiment. We use the output of a mode-locked Ti:sapphire laser at a wavelength of 800 nm, with a pulse width of 200 fs and a repetition rate of 80 MHz, which corresponds to 12.5 ns between pulses. The power per pulse emitted from the Ti:sapphire oscillator cavity is around 15 nJ, and the total beam power is approximately 1 to 1.5 W. A polarizing beam splitter separates pump from probe, and a half wave plate dictates how much power goes into each. Typically, about 95 to 97 percent of the energy is sent into the pump beam with the rest going into the probe.

The probe is sent though a mechanical delay stage. The length of our stage provides a maximum of 7 ns delay between pump and probe beams. In order to mitigate alignment issues of the pump and probe on the sample due to the motion of the delay stage, we expand the probe beam diameter by a factor of four before sending it through the delay stage, and then re-compressed it before focusing it onto the sample. Emitted light from the oscillator cavity is not perfectly collimated, and expanding the beam reduces its divergence over the long delay. The probe is focused onto the sample at normal incidence using a 10x microscope objective. Due to losses in optics, the probe power incident on the sample is generally around 10 mW. The reflected probe light is focused into a PIN diode detector, whose signal is fed into the lock-in detector. An inductance resonator is placed between the photodiode and the lock-in to boost the signal-to-noise ratio as discussed above.

After the initial polarizing beam splitter, the pump is sent into an electro-optic modulator (EOM), which modulates the beam at a specified reference frequency (typically 1 to 15 MHz). The reference frequency is also fed into a lock-in detector, and is used to detect the small values of reflectance change due to surface heating of the sample by the pump. The reference frequency is supplied to the EOM and to the lock-in by a function generator, and is chosen to match the resonance frequency of the inductive resonator.

In order to separate pump from probe, we use second harmonic generation (SHG) to frequency double the pump using a bismuth triborate (BIBO) crystal, which converts the pump wavelength from 800 nm to 400 nm. The pump is then focused onto the sample co-axially with the probe. Due to losses, primarily in the EOM and the BIBO crystal, the pump beam power incident on the sample is typically less than 120 mW. The reflected pump light is filtered out using color-specific filters such that none of it enters the detector. Even a small amount of pump light at the reference frequency would totally overwhelm the signal from much smaller probe.

The diameter of the focused probe beam is typically 10 μm, while the diameter of the focused pump beam is chosen to be between 20 and 100 μm. For measurements of cross-plane thermal properties, It is advantageous for the probe to be kept much smaller than the pump to minimize effects from radial conductance. To study in-plane thermal properties, the pump and probe can be chosen to have more similar diameters, which will increase the sensitivity to radial conduction effects [40]. In all measurements, the probe must be sufficiently small compared to the pump to eliminate errors in overlap of the pump and probe beams on the sample at different delay times.

We use a charged coupled device (CCD) camera, ring light and removable mirror to create a microscope for visualizing the sample surface. This allows us to reliably place the sample surface at the focal plane of the 10x microscope objective where we measure the focused pump and probe beam diameters, and to visually select which regions on the sample to measure.

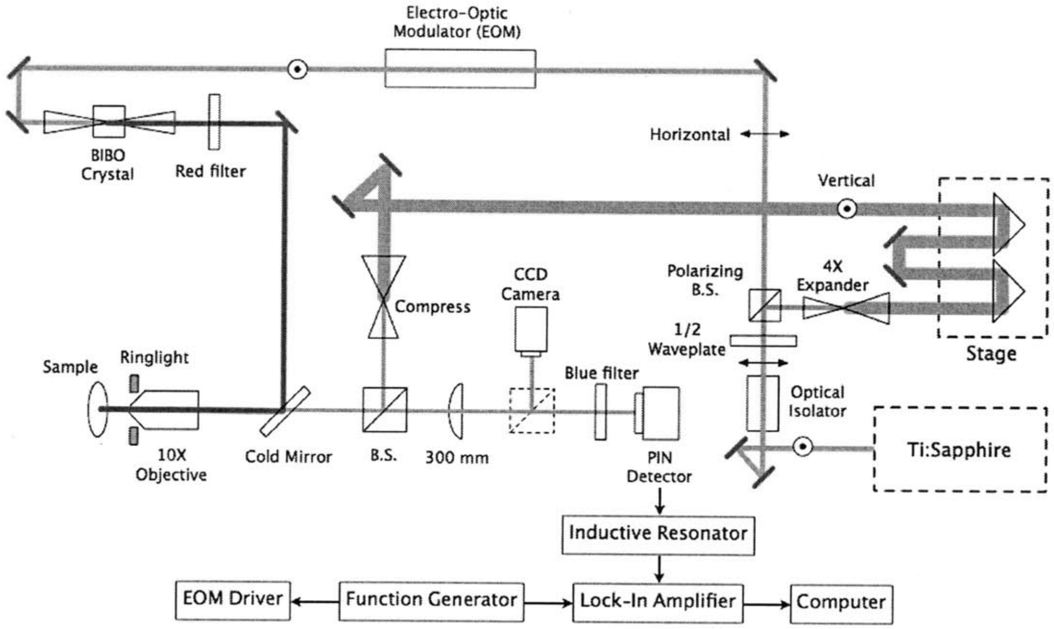
Electro-Optic Modulator (EOM)
Horizontal
BIBO Crystal
Red filter
Vertical
Polarizing B.S.
4X Expander
CCD Camera
Compress
1/2 Waveplate
Stage
Sample
Ringlight
Blue filter
Optical Isolator
Ti:Sapphire
10X Objective
Cold Mirror
B.S.
300 mm
PIN Detector
Inductive Resonator
EOM Driver
Function Generator
Lock-In Amplifier
Computer

Figure 2-3: Diagram of optical components and major electronic components of TTR experimental setup developed by A. Schmidt. Figure adapted from [28].

Many of the features of our TTR system were inspired by the work of Cahill and coworkers as discussed above, but notable improvements have been made. While other TTR systems separate pump and probe by sending them onto the sample at different angles [25, 26], and some use polarization differences [27], our method of SHG has several advantages. The different angle approach presents alignment and overlap challenges, and risks scattering of pump light in the probe direction due to surface roughness. The polarization method is also sensitive to surface conditions on the sample which cause the polarization of the reflected light to differ from the incident light. SHG allows for co-axial alignment of the pump and probe beams at normal incidence to the sample surface, which greatly simplifies alignment challenges and makes the measurement less sensitive to roughness on the sample surface.

2.2.1 Model for Data Analysis

The measured change in reflectance is related to a thermal model for radial anisotropic heat flow through layered structures in order to extract thermodynamic properties of the sample. First, a transfer function relates the output of the lock-in amplifier to the input of the probe beam to the PIN detector. Then, a model relates the change in the surface temperature of the sample due to the pump beam heating to the thermal properties of the sample. Here we present the important formulas and refer the reader to Ref. [28] for a full derivation.

The lock-in mixes the signal from the PIN detector with the reference frequency from the function generator to produce in-phase, X, and out-of-phase, Y, signal components. The magnitude, R, and phase, ϕ, of the signal are related to these signal components through Eqns. (2.7) and (2.8).

$$R = \sqrt{X^2 + Y^2} \tag{2.7}$$

$$\phi = \tan^{-1}(Y/X) \tag{2.8}$$

The signal amplitude and phase reported by the lock-in relate to the probe input to the PIN diode through the real part of Eqn. (2.9), where ω_o is the pump modulation frequency set by the EOM and $Z(\omega_o)$ is a transfer function describing the thermal response of the sample. Since an analytical solution of the sample response is more simple in the frequency domain, only the frequency domain solution will be discussed here, although both frequency and time domain solutions are presented in Ref. [28].

The transfer function in the frequency domain is given by Eqn. (2.10), where β is a constant related to the thermoreflectance of the surface and electronic gains in the system, Q and Q_{probe} are the energies of the pump and probe pulses respectively, T is the period between pulses (which is 80 MHz for our system), τ is the delay time between pump and probe pulses (which is between 0 and 7 ns for our system), and $H(\omega)$ is the sample frequency response. Equation (2.10) together with Eq. (2.9) provide a general expression describing the signal returned by the lock-in. In the limit of no accumulative heating, when pulses are spaced far enough apart that the surface cools completely before the next pulse arrives ($T \to \infty$), $Z(\omega_0)$ reduces to the impulse response solution.

$$Re^{i(\omega_o t+\phi)} = Z(\omega_o)e^{i\omega_o t} \tag{2.9}$$

$$Z(\omega_0) = \frac{\beta Q Q_{probe}}{T^2} \sum_{k=-\infty}^{\infty} H(\omega_o + 2\pi k/T)e^{i2\pi k\tau/T} \tag{2.10}$$

To find an expression for the frequency response of the sample, $H(\omega_o)$, we use an analytical solution for one dimensional heat diffusion in layered structures and generalize it to account for radial conduction. Figure 2-4 depicts a general layered structure, with Θ_{top} and f_{top} describing the temperature and heat flux on the top surface respectively, and Θ_{bottom} and f_{bottom} describing the temperature and heat flux respectively on the bottom surface. Each layer is assigned a number, with 1 representing the top layer and n representing the bottom layer. The cross-plane direction is defined as the z direction.

Each layer is described by a matrix of material properties, M_n, as shown in Eq. (2.11). Here d is the layer thickness and q is given by Eq.(2.12), where σ_z and σ_r are the cross-plane and radial thermal conductivities respectively, ρ is the density, c is the specific heat, and k is the transform variable. The effects of radial conduction have been accounted for in Eqns. (2.11) and (2.12). Interfaces between materials are also represented as "layers". The material property matrix for interfaces, $M_{n,int}$, is shown in Eq. (2.13), where G is the thermal interface conductance.

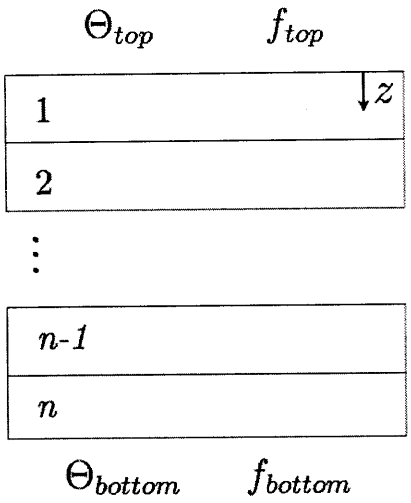

Figure 2-4: Diagram of layered sample. Pump and probe beams are incident on the top surface. Figure adapted from Ref. [28].

$$M_n = \begin{bmatrix} \cosh(qd) & \frac{-1}{\sigma_z q}\sinh(qd) \\ -\sigma_z q \sinh(qd) & \cosh(qd) \end{bmatrix} \tag{2.11}$$

$$q^2 = \frac{\sigma_r k^2 + \rho c i \omega}{\sigma_z} \tag{2.12}$$

$$M_{n,int} = \begin{bmatrix} 1 & G^{-1} \\ 0 & 1 \end{bmatrix} \tag{2.13}$$

The top and bottom surface temperatures and heat fluxes are related through the product of the individual layer matrixes as shown in Eq. (2.14). If an adiabatic boundary condition is assumed on the bottom surface ($f_{bottom} = 0$), the top surface temperature and heat flux are related through Eq.(2.15). Assuming an adiabatic boundary condition on the bottom surface implies that the n^{th} layer can be considered infinitely thick, as far as the conduction heat transfer is concerned. All of the samples we investigate satisfy this boundary condition.

$$\begin{bmatrix} \Theta_{bottom} \\ f_{bottom} \end{bmatrix} = M_n M_{n-1} ... M_1 = \begin{bmatrix} A & B \\ C & D \end{bmatrix} \begin{bmatrix} \Theta_{top} \\ f_{top} \end{bmatrix} \tag{2.14}$$

$$\Theta_{top} = \frac{-D}{C} f_{top} \tag{2.15}$$

The thermal frequency response of the system is given by Eq. (2.16), where A is the amplitude of the absorbed laser power, w_0 and w_1 are the pump and probe $1/e^2$ radii respectively, and C and D are matrix elements of material properties from Eq. (2.14). This integral is solved numerically varying unknown material properties to match measured data.

$$H(\omega) = \frac{A}{2\pi} \int_0^\infty k\left(\frac{-D}{C}\right) exp\left(\frac{-k^2(w_0^2 + w_1^2)}{8}\right) dk \tag{2.16}$$

Quite commonly, samples are comprised of two material layers and an interface (three layers total for the thermal model). The unknown thermodynamic parameters are often the thermal conductivity of the bottom layer and the thermal interface conductance.

2.2.2 Sample Preparation

The top layer of samples measured using TTR generally consists of a metal film. This film both absorbs the laser light and acts as a temperature transducer due to its change in reflectance, as discussed in Sec. 2.1.1. Often, for our TTR measurements, we choose to use aluminum for the transducer film because the peak in the thermoreflectance coefficient of Al is well matched to the 800 *nm* wavelength of our probe beam [41], leading to a high signal-to-noise ratio. Metal films are typically either sputter deposited or electron beam (e-beam) deposited onto a sample surface.

Table 2.1 shows the room temperature optical absorption depths for different metals at 400 *nm* and 800 *nm* [42]. The thickness of the metal film should be several times greater than the optical absorption depth.

Several methods exist for characterizing the thickness of the deposited film. If sufficient acoustic mismatch exists between the film and the underlying substrate, the subpicosecond time resolution of our TTR measurement enables the observation of acoustic echos off the metal-substrate interface. Figure 2-5 shows a TTR signal

Table 2.1: Room temperature optical absorption depths in *nm* for various metals at wavelengths of 400 *nm* and 800 *nm*. All data from Ref. [42]

Material	400 *nm*	800 *nm*
Ag	16.324	12.037
Al	6.5827	7.6202
Au	16.274	12.441
Co	10.603	13.510
Cr	11.166	18.399
Cu	13.539	12.647
Ir	9.5018	12.171
Li	19.480	16.816
Mo	9.8854	18.966
Ni	13.488	14.535
Os	7.5583	38.235
Pd	10.803	12.498
Pt	11.206	12.856
Rh	7.5788	9.3618
Ta	13.972	18.055
Ti	14.804	19.193
V	9.4174	20.138
W	13.208	23.317

for aluminum on silicon. The inset zooms in on the first 200 *ps* of data in which the acoustic echos are clearly visable. These echos result from the rapid temperature rise in the metal film, which generates a thermal expansion stress wave that reverberates through the film [14]. Using the speed of sound in the metal film, the film thickness can be determined from the period of these oscillations. In practice, however, we find that echos are often too weak or too few to be a reliable method of determining film thickness.

Another method for determining film thickness is to mask a portion of the sample during deposition, and later use profilometry methods to measure the deposited thickness. However, many contact profilometers are not sensitive enough to provide the required nanometer resolution. The thickness of the metal film is a critical parameter in the thermal model, and thickness inaccuracies of a few *nm* could produce noticeably different data fitting results. Atomic force microscopy (AFM) would provide a more sensitive measurement, but in addition to being time consuming, the

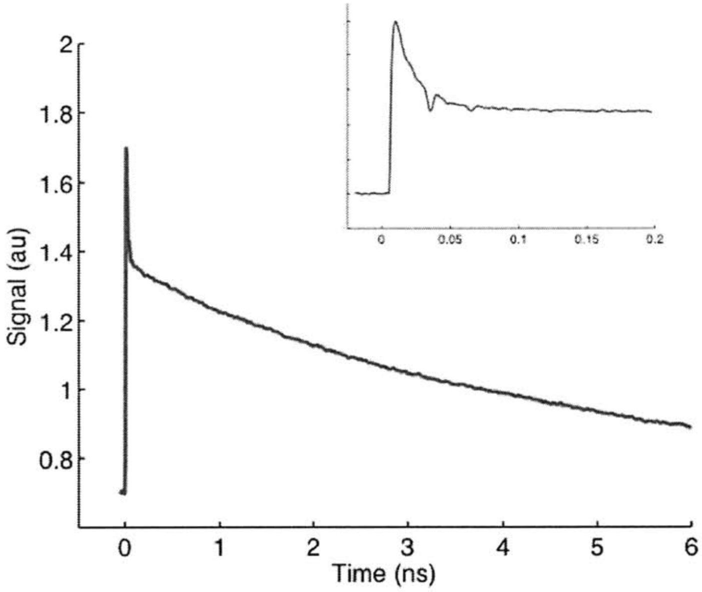

Figure 2-5: Typical TTR signal for a sample of Al on Si. Inset enlarges the first 200 *ps* of data in which acoustic echos off the Al-Si interface are detected.

AFM used would need to have a sufficiently long lateral scanning ability. Masking the sample during film deposition inevitably results in a thinner film near the edge of the masked region, so any profilometer or AFM would need to travel the distance from substrate region to the region of maximum film thickness.

We find that an accurate and simple way to characterize the film thickness in most instances is to include a calibration material near the sample during the deposition. Often, we chose to use a piece of a polished single crystal sapphire wafer as a calibration material. To determine the deposited film thickness, we use TTR to measure the sapphire, and since the thermal properties of the sapphire are well known, we allow the unknown metal film thickness to vary when fitting the measured TTR data. In practice we find that the film thicknesses determined in this manor agree well with thicknesses determined using other more time consuming methods like profilometry.

If a sample surface is rough, polishing may be required before a reliable TTR measurement is possible. Although our SHG scheme for distinguishing pump and probe allows us to be far less sensitive to surface roughness than other TTR systems, large roughness can cause the thickness uniformity of the deposited metal film to vary significantly. Without an accurate way of knowing the film thickness at the measurement location, it is not possible to reliably fit TTR data, resulting in large variations in fitted properties from one measurement location to the next. In order to obtain a uniform metal film, the roughness of the sample must be much less than the film thickness, which is generally on the order of 50 to 150 *nm*.

In the mechanical polishing of rough samples, minimizing subsurface damage is important for the consistency of TTR results [1], because the thermal depth probed in the sample is limited. If the damaged region is a significant portion of the probed region, the measured thermal properties will reflect the damaged region, rather than the bulk. Mechanical polishing techniques can result in a subsurface damage region with a thickness a factor of two larger than the abrasive size used [43], or a factor of two larger than the peak-to-valley surface roughness [44]. Thus, initial polishing using large abrasive sizes can result in a substantial subsurface damage region, which must be removed with subsequent polishing using smaller particles. Removal of large depths of subsurface damage using small particle abrasives is a time consuming process, but one which is critical for accurate material characterization using TTR techniques.

2.2.3 Temperature Dependent TTR

We have advanced our TTR system beyond that discussed in Ref. [28], to be able to measure samples at temperatures other than room temperature. In this section, we discuss some of the major elements of our cryogenic system. Samples are mounted in a Microstat HE Cryostat from Oxford Instruments that is capable of achieving temperatures ranging from liquid helium temperatures (4 K) to 350 K. For this thesis, only temperatures down to liquid nitrogen temperatures (77 K) have been explored.

A BOC Edwards turbo pump station is used to evacuate the cryostat, and achieves pressures of $2\text{x}10^{-5}$ *Torr* or better at room temperature after a relatively short pumping time of roughly 20 minutes. Isolating the cryostat from the vibrations of the pumping station is critical. The sample surface must remain in focus, and the pump and probe beams must remain in the same location on the sample, throughout the duration of the measurement. We achieve very effective vibration isolation by sandwiching the vacuum hose between bags of dry rice and anchoring the bags to a stationary structure.

Figure 2-6 shows a schematic of the lower portion of the cryostat where the sample is mounted. Proper thermal mounting of the sample holder onto the cold finger, and the sample onto the sample holder, is essential for achieving the lowest possible sample temperatures. We use a single sheet of indium foil at each of these junctions to fill micro voids and provide good thermal contact.

We found that thermocouples did not provide reliable temperature measurements at cryogenic temperatures because of a substantial temperature gradient across the electrical pins from the inside to the outside of the cryostat, which resulted in an offset in the measured temperature. Instead, to measure the sample temperature, we use a silicon diode mounted to the sample surface using a very thin layer of Apieason thermal grease. The leads of the silicon diode are thermally anchored by being wrapped several times around the base of the cold finger.

In spite of low pressures and long pump times, we still observed vapor condensation and freezing on the sample surface. Any ice crystals on the sample greatly disrupt the reflectivity measurement. To prevent condensation on the sample, we affix a thin glass microscope slide onto the outside of the radiation shield as shown in Fig. 2-6. The glass slide is thin enough that it does not contact the walls of the cryostat. The radiation shield is thermally anchored to the base of the cold finger, thus the temperature of the glass slide will be similar to that of the sample, or even a little colder. By making the gap between the glass slide and the sample surface small, vapor in the chamber tends to condense on the cold glass, rather than on the sample surface.

2.3 Summary

We have provided an overview of transient thermoreflectance (TTR) experiments including our own, designed by Aaron J. Schmidt as part of his Ph.D. work at the

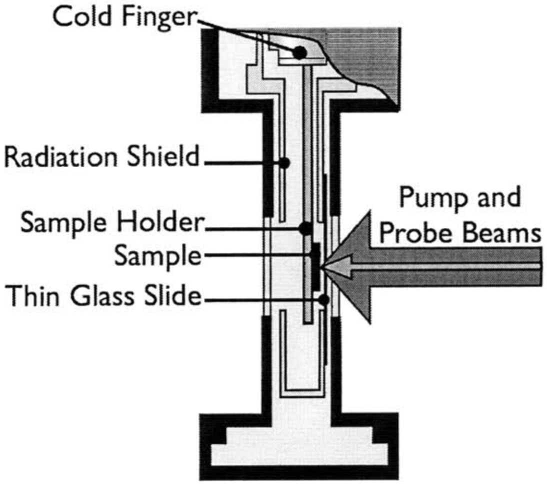
Cold Finger
Radiation Shield
Sample Holder
Sample
Thin Glass Slide
Pump and
Probe Beams

Figure 2-6: Close up schematic of cryostat showing sample mounted to cold finger with a thin glass slide to collect condensation. Figure adapted from promotional images at oxford-instruments.com.

Massachusetts Institute of Technology. For further details regarding our experimental system or thermal modeling, the reader should refer to Schmidt's Ph.D. thesis [28]. In the next two chapters, we present experimental studies of thermal interface carried out on our TTR system.

Chapter 3

Thermal Conductance at Metal-Graphite Interfaces

3.1 Motivation and Background

Nanoscale systems that incorporate carbon materials have become increasingly interesting for both fundamental and practical applications. Carbon nanotubes (CNTs) and graphenes represent two large areas of research due to their unique dimensionality and resulting physical properties [45, 46, 47, 48]. Thermal interface materials made of metal-graphite composites have also gained attention [49, 50], making the understanding of heat transport at metal-graphite interfaces crucial. In order to characterize the thermal properties of CNTs, it is necessary to involve metal contacts, and hence the finite thermal conduction resistance at the contacts must be quantified in order to obtain accurate property measurements [51, 52, 53].

It has been shown theoretically by Prasher that the thermal interface conductance between metal and the cross-plane (c-axis) direction of graphite is an excellent approximation to the interface between metal and the sidewall of a multiwalled carbon nanotube (MWCNT) [53]. Very little data has been reported for the thermal interface conductance between metal and graphite [40]. Some studies have considered the thermal interface conductance at metal-diamond interfaces [15, 54]. The thermal conductance per unit length between a single walled CNT and SiO_2 was estimated by Pop et al. to be approximately 0.17 W/mK, or depending on contact area around 1 x 10^8 W/m^2K [55], and Maune et al. found a similar result [56].

Here we use TTR techniques to measure the thermal interface conductance between highly ordered pyrolytic graphtie (HOPG) and metal films of Al, Au, Cr, Ti, and Al with a 5 nm Ti stiction layer (referred to as Al/Ti), over a temperature range from 89 K to 300 K. Measurements of the room temperature thermal interface conductance for Ag, Ni and Sn on graphite are also discussed.

3.2 Samples

Samples of HOPG were obtained from SPI corporation and from the Dresselhaus group at MIT. HOPG is a form of high purity graphite with large single crystal regions displaying in-plane atomic smoothness. In the basal plane, carbon atoms form a hexagonal structure with strong sp^2 covalent bonding. Much weaker bonds hold the planes together, allowing the planes of graphite to be easily separated. We cleaved our samples of HOPG using the standard double-sided tape method. Double-sided carbon tape was pressed onto the HOPG surface and then pealed off. The result was a freshly exposed graphite basal plane several mm in size, which we then coated in metal.

We investigate the temperature-dependent thermal interface conductance between HOPG and a range of metals: Al, Au, Cr, Ti, and Al with a 5 nm Ti adhesion layer (referred to as Al/Ti). All films were created through electron-beam (e-beam) deposition at a rate of 1.5 $\AA/s$. Each film was approximately 90 nm thick. Film thicknesses were determined by calibration to a sample of single crystal sapphire with a known thermal conductivity that was coated simultaneously with the graphite. A scanning electron microscope (SEM) was used to image the surface of the deposited films. Figure 3-1 shows the SEM images.

From the SEM images, a clear difference exists in the film quality and coverage for different metals on HOPG. Both the Al and Ti films formed continuous coatings. The Au film, however showed characteristic pocketing, indicative of poor adhesion

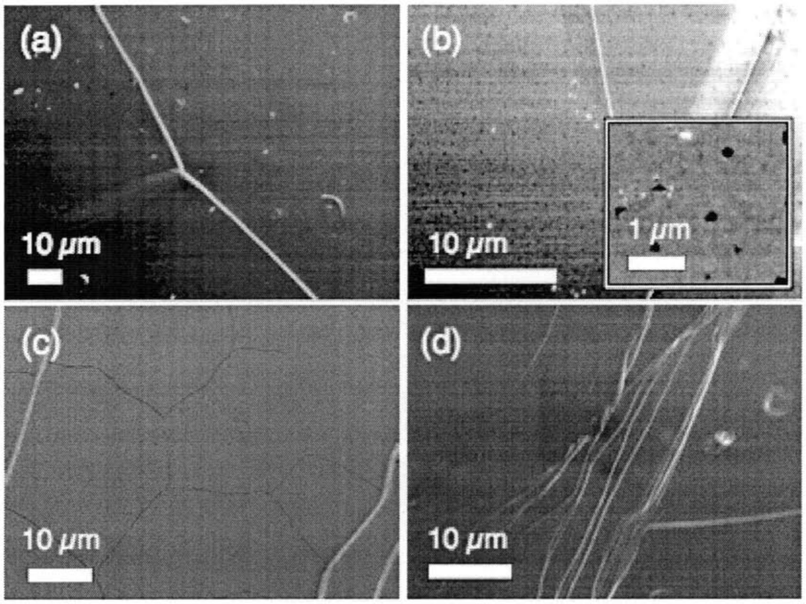

Figure 3-1: SEM images of HOPG samples coated in (a) Al, (b) Au, (c) Cr and (d) Ti.

[57]. We observed this same pocketing behavior using both e-beam and sputtering deposition techniques. The Cr was also not as continuous as the Al and Ti films, forming grains on the order of tens of microns. Large-scale cracks in the images are simply cracks in the HOPG that resulted from the cleaving process. Regions without cracks were larger than the diameter of our pump and probe beams, allowing us to avoid these large-scale cracks during our measurement.

Graphite is an extremely anisotropic material with a room temperature cross-plane thermal conductivity of around 5 to 10 W/mK and an in-plane thermal conductivity comparable to that of diamond, around 2000 W/mK. In this study, we primarily investigate the cross-plane transport properties by using a much larger pump spot diameter (80 μm) as compared to the probe spot diameter (10 μm). We also used a pump modulation frequency on the order of 10 MHz. Our thermal analysis accounted for the anisotropic properties of graphite by using literature values of in-plane thermal conductivity as a function of temperature. Measuring in-plane properties of a highly anisotropic material is possible using TTR [40], but was outside the scope of this work. We refer to the cross-plane direction in graphite as the c-axis, while referring to in-plane loosely as the a-axis.

3.3 Results

Figure 3-2 shows typical scaled room temperature thermal reflectance signals for each metal-graphite pair. The inset shows the first 200 *ps* of data in which acoustic echos off the metal-graphtie interface are apparent. A clear difference exists in the shape of the decay curves for each case. Not only the long-term decay, but also the decay of the initial hot electron peak is distinct for each case.

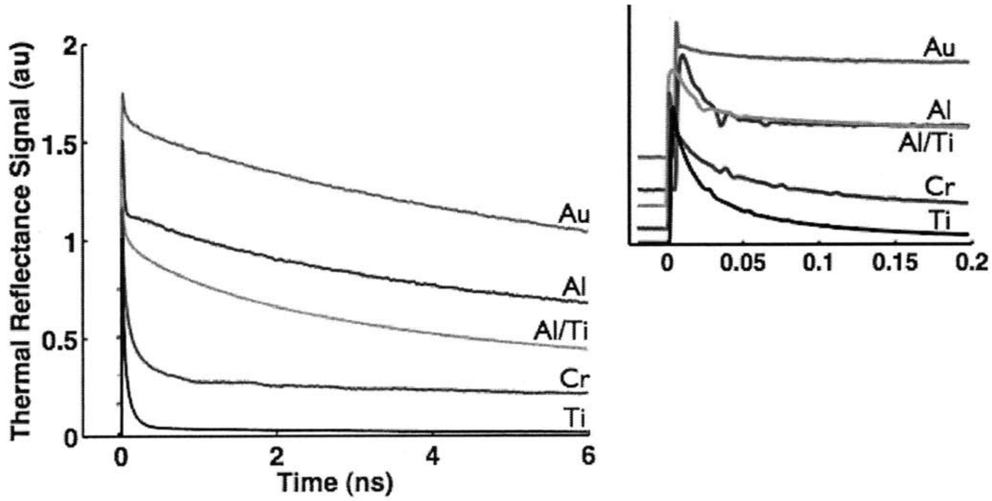

Figure 3-2: Scaled room temperature thermoreflectance signals for various metals on HOPG. Inset shows the first 200 *ps* of data in which acoustic echos off the metal-diamond interface are apparent.

The measured results for the thermal interface conductance, G, at metal-graphite interfaces as a function of temperature are shown in Fig. 3-3. Thermal interface conductance increases with increasing temperature as expected [1]. Au displayed the lowest conductance with graphite over the entire temperature range, followed by Cr, Al, and finally Ti and Al/Ti, which displayed the highest conductance. The plotted points represent average results. For all data, except the Ti data, the deviation was approximately ±20%. This larger range of deviation stems from the low value of

HOPG cross-plan thermal conductivity. The conduction resistance in HOPG contributes to the heat transport, making the measurement less sensitive to the interface resistance as compared to high thermal conductivity substrates. Temperature at the sample surface was determined using a Si diode affixed to the sample. We estimate the uncertainty in the temperature, including steady state laser heating effects, to be less than $\pm 1K$.

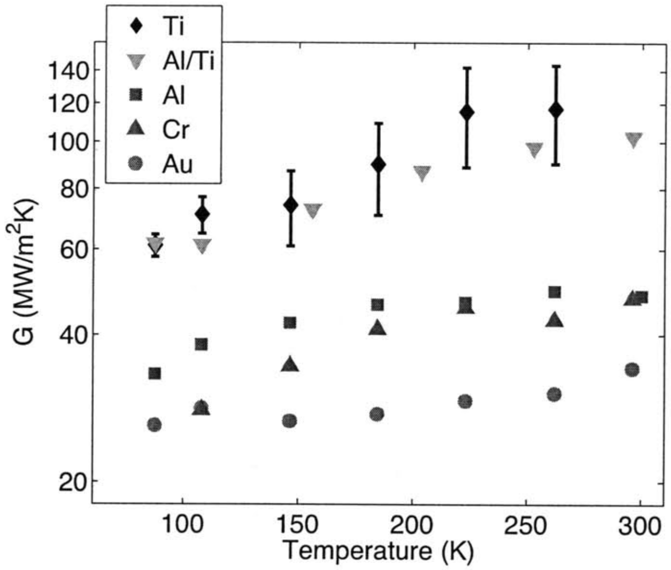

Figure 3-3: Measured thermal interface conductance values, G, for various metals on HOPG as a function of temperature. Measurement was in the c-axis direction. The metals considered were Al, Au, Cr, Ti and Al with a 5 nm Ti adhesion layer, designated Al/Ti.

The reflectance data for Ti became increasingly noisy at higher temperatures. The bars on the Ti data indicate the standard deviation of the measured data. At room temperature, a reasonable result could not be achieved. We suspect the difficulty in measuring Ti stemmed from a weak thermoreflectance coefficient at our probe wavelength. In order to gain further confidence in our results, we measured a sample of HOPG coated in an 80 nm Al film with a 5 nm Ti stiction layer. The results for Al/Ti were repeatable to within ±20%. In our model we neglected any thermal resistance at the interface between Al and Ti, an approximation that we expect is reasonable given that Al and Ti have comparable phonon velocities and that metal-

metal interfaces have much higher thermal conductance values than metal-nonmetal interfaces [58].

We also measured room temperature thermal interface conductance values for silver, tin and nickel on HOPG. The room temperature G values for all metals considered are plotted in Fig. 3-4 as a function of the metal's Debye temperature. Again, we plot average measured values for G, and the results deviated by approximately ±20%.

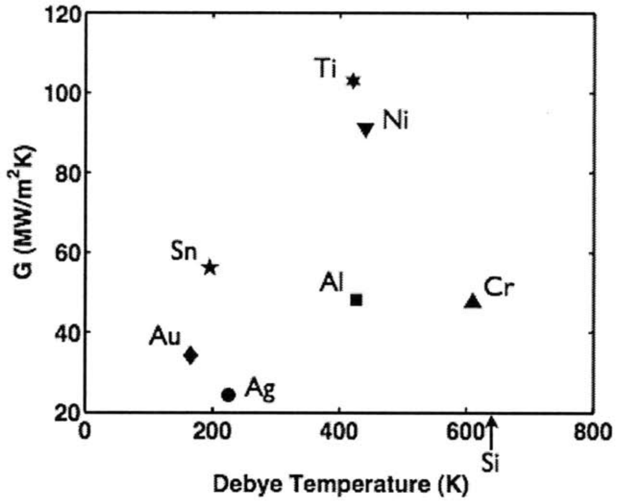

Figure 3-4: Measured room temperature thermal interface conductance values, G, for various metals on HOPG plotted as a function of the Debye temperature of the metal.

A material's Debye temperature, T_D, can be related to its Debye cutoff frequency, ω_D, by the simple relation in Eq. (3.1), where $\hbar$ is Plank's constant divided by 2π and k_B is Boltzmann's constant.

$$T_D = \frac{\hbar\omega_D}{k_B} \tag{3.1}$$

The Debye frequency for graphite is higher than for any of the metals considered. Thus, in model calculations of G, the frequency cutoff used is that of the metal. There may be a slight upward trend in measured values of thermal interface conductance with increasing Debye temperature, but the trend is not definitive. Some of the discrepancy may be due to the differences in adhesion of the metal films onto the HOPG surface, as evidenced by the SEM images in Fig. 3-1. It has been shown that the acoustic mismatch model may be adapted to account for adhesion energy at the interface, and that the strength of the adhesion energy influences the predicted thermal interface conductance in the case of weak bonding [19].

3.4 Modeling

We calculate the diffuse mismatch model, DMM, predictions to compare with our results. Since our experiment was conducted at higher temperatures than a few K, we expect phonons to have shorter wavelengths approaching the scale of the atomic scale roughness at the interface, and thus phonon scattering should be more diffuse. We use Eq. (1.6), considering medium 1 to be the metal and medium 2 to be the graphite. The central assumption of the DMM is that transmissivity is independent of angle, giving Eq. (1.14). Under this assumption, Eq. (1.6) simplifies to

$$G = \sum_j \frac{1}{4} \int_0^{\omega_1^{max}} v_1 C_1(\omega) \alpha_{1\to 2}(\omega) d\omega \tag{3.2}$$

But, since we are using a Fourier heat conduction model, we would like to account for an equivalent equilibrium temperature, which is a better representation of the local energy density near the interface. Thus, we use the corrected form of G given in Eq. (1.10). Again, by assuming $\alpha_{1\to 2}$ independent of angle, Eq. (1.10) simplifies to Eq. (3.6) as follows.

$$G = \sum_j \frac{\frac{1}{4} \int_0^{\omega_1^{max}} v_1 C_1(\omega) \alpha_{1\to 2}(\omega) d\omega}{\left[1 - \frac{1}{2}\left\langle \int_0^1 \alpha_{1\to 2}(\omega) d\mu_1 + \int_0^1 \alpha_{2\to 1}(\omega) d\mu_2 \right\rangle\right]} \tag{3.3}$$

$$G = \sum_j \frac{\frac{1}{4} \int_0^{\omega_1^{max}} v_1 C_1(\omega) \alpha_{1\to 2}(\omega) d\omega}{\left[1 - \frac{1}{2}\left\langle \alpha_{1\to 2}(\omega) + \alpha_{2\to 1}(\omega) \right\rangle\right]} \tag{3.4}$$

$$G = \sum_{j} \frac{\frac{1}{4} \int_{0}^{\omega_1^{max}} v_1 C_1(\omega) \alpha_{1\to 2}(\omega) d\omega}{\left[\frac{1}{2}\right]} \tag{3.5}$$

$$G = \sum_{j} \frac{1}{2} \int_{0}^{\omega_1^{max}} v_1 C_1(\omega) \alpha_{1\to 2}(\omega) d\omega \tag{3.6}$$

Effectively, accounting for the equivalent equilibrium temperature has added a factor of 2 to the model. We also make the usual DMM assumption that the scattering is elastic, and take ω^{max} to be the Debye frequency in the metal, which represents the lower of the Debye frequencies in either medium. Metal Debye frequencies are calculated from literature values of Debye temperature [59]. By lumping together the three phonon polarizations (one longitudinal and two transverse), the phonon transmissivity under the DMM is given by Eq. (1.18).

For the phonon dispersion relation in the metal, we assume a sine-type dispersion relation which gives a more accurate representation of the real dispersion relation at higher temperatures than a linear Debye model. For the graphite dispersion relation, we follow the approach of Duda et. al, and use an effective two dimensional density of states, which is a superior approximation to the physical density of states in graphite than a three dimensional model [11].

Figure 3-5 compares the measured thermal interface conductance results to the calculated prediction of the DMM. Since we measure cross-plane transport, for the calculation we used the velocities of c-axis phonons on the graphite side, and refer to this calculation as the "c-axis model."

From Fig. 3-5 it is clear that the DMM assuming c-axis graphite phonon velocities under predicts the measured data in almost every case. Differences in the initial decay profiles of the hot electrons shown in Fig. 3-2 suggest differences in the relaxation dynamics of the electrons in the various metals. To rule out the possible influence of electron-phonon coupling in the metal, we follow the approach of Majumdar and Reddy [20] discussed in Sec. 1.1.3. Since values for the phonon contribution to the thermal conductivity of metals are scarce in the literature, we only calculate the

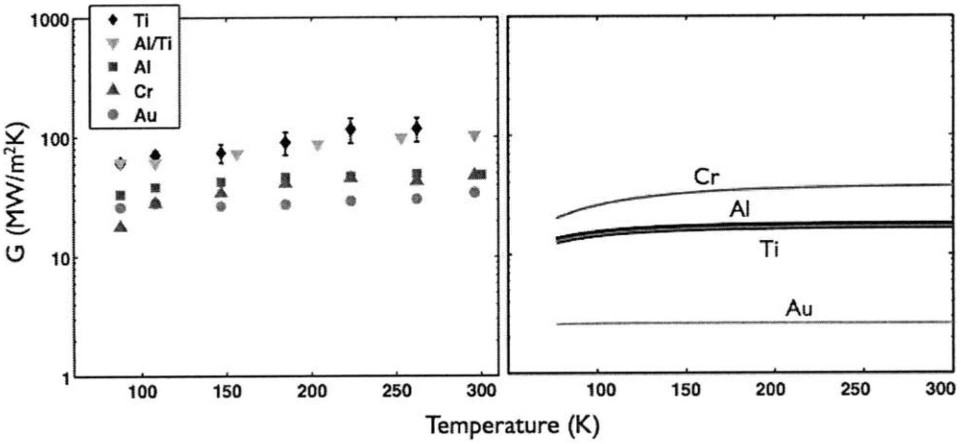

Figure 3-5: Measured thermal interface conductance data compared to DMM results assuming only contributions from c-axis phonon velocity on the graphite side. Model predictions for Al on graphite are almost identical to model predictions for Ti on graphite.

thermal interface conductance predicted by Majumdar and Reddy's model at room temperature for Al and Au. Table 3.1 lists the values of electron-phonon coupling constants and phonon thermal conductivities we used, and Table 3.2 compares the calculated results from Majumdar and Reddy's model to the calculated DMM results plotted in Fig. 3-5. The similarity between Majumdar and Reddy's model and the DMM predictions suggests that electron-phonon coupling in the metal is not significant.

Table 3.1: Room temperature values of bulk electron-phonon coupling constants, $G_{coupling}$, for Al and Au from Ref. [60]. Room temperature values for phonon thermal conductivity, k_p, were calculated using molecular dynamics simulations [61].

Material	$G_{coupling}$ $[10^{16} W/m^3K]$	k_p $[W/mK]$
Al	24.5	16.1
Au	2.9	3.4

One possible explanation for the under prediction of the DMM is the assumption that phonons from the metal side only couple to c-axis phonons on the graphite side. One implicit assumption of the DMM is that there be some level of interfacial roughness that causes diffuse scattering. Even though HOPG is very smooth, the way the metal film forms on the surface could have resulted in atomic scale roughness

Table 3.2: Comparison of the calculated thermal interface conductance based on the model of Majumdar and Reddy [20], G^*, which accounts for electron-phonon coupling in the metal to the DMM, G_{DMM}, which only accounts for phonon-phonon coupling at the interface.

Sample	G^* $[MW/m^2K]$	G_{DMM} $[MW/m^2K]$
Al/HOPG	17.07	17.22
Au/HOPG	2.61	2.63

features at the interface. Phonons with wavelengths on the same order as these roughness features would be able to transmit some of their momentum in the a-axis direction. In the basal plane of graphite, phonon velocities are much higher than across the basal plane. Thus, even a small amount of coupling to in-plane velocities would result in a large difference in the predicted interface conductance. In Fig. 3-6 we show a DMM calculation assuming a weighted average of in-plane and cross-plane phonon velocities in graphite, referred to as "average model." Since knowing the exact morphology of the interfaces at an atomic scale is not experimentally viable, for the average model we assume an equal weighting between in-plane and cross-plane velocities for each case given by $1/2\sqrt{v_c^2 + v_a^2}$.

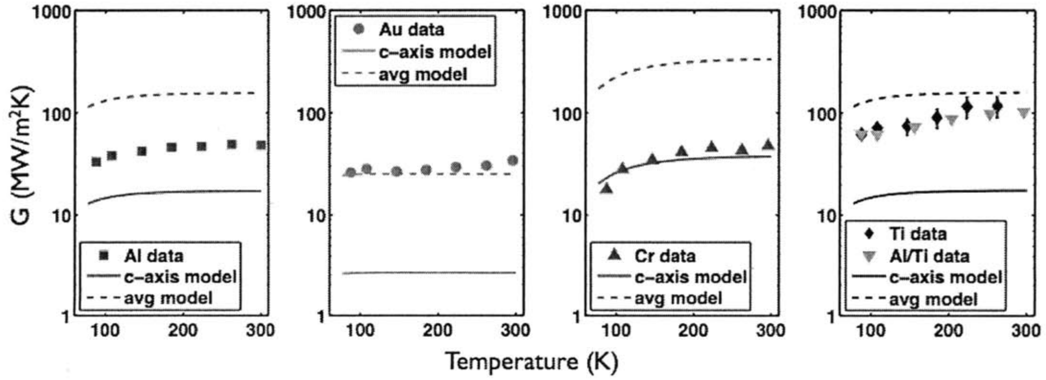

Figure 3-6: Measured thermal interface conductance data compared to DMM results. Calculated results shown assuming only c-axis phonon velocities (c-axis model), and assuming an average of a-axis and c-axis phonon velocities (avg model) in the graphite.

Due to the extreme anisotropy of graphite, the average model predicts a significantly higher thermal interface conductance than the c-axis model. The scale of the interfacial roughness, and thus the degree of coupling to in-plane phonons, should depend on the type of metal deposited. Thus, if it were possible to base the weighting on the interfacial morphology, a greater insight into the merits of this theory would be possible.

3.5 Comparison to Diamond

To gain further insight, we compare our results for metal on graphite to published results for metal on isotropically enriched diamond interfaces [54], as shown in Fig. 3-7.

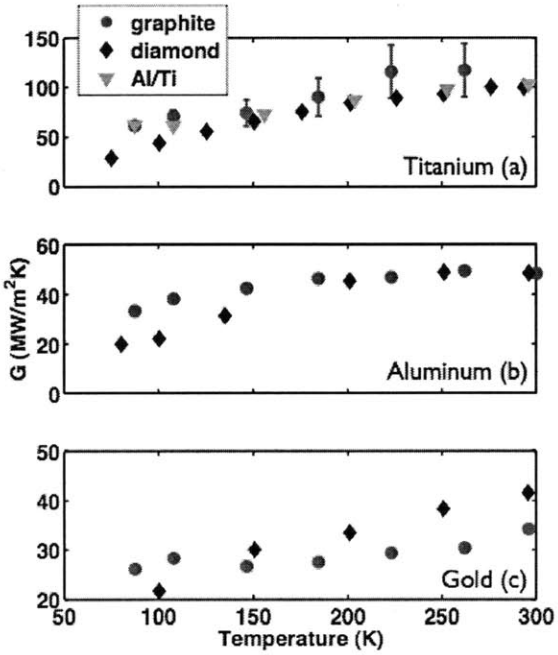

Figure 3-7: Measured thermal interface conductance data compared to literature metal-on-diamond results from [54].

Diamond is a cubic crystal with strong sp^3 covalent bonds. The phonon velocities in diamond are comparable to those in the basal plane of graphite. Surprisingly, the thermal interface conductance values are similar for both metal-graphite and metal-diamond interfaces. This similarity supports the notion that in-plane phonons in the graphite are contributing to transport. Additionally, the metal-HOPG interface conductance values may have a slightly weaker temperature dependance than the metal-diamond conductance values, a phenomenon predicted by the DMM which results from the graphite density of states being modeled as effectively two dimensional. Figure 3-8 shows DMM calculations for the aforementioned c-axis and average models as well as calculations assuming the velocity of only in-plane phonons referred to as the "a-axis" model and calculations for diamond.

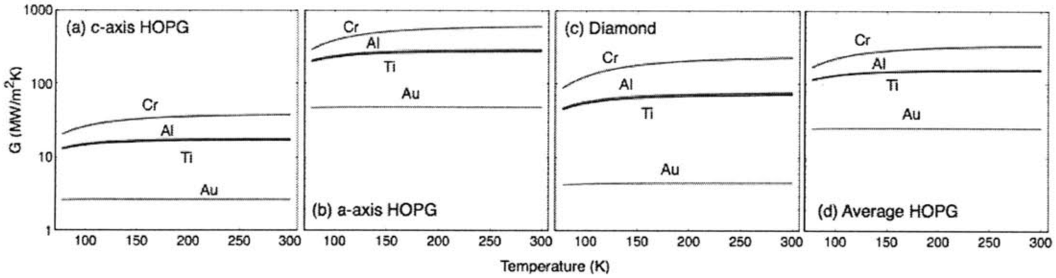

Figure 3-8: DMM calculations for the thermal interface conductance between various metals and (a) c-axis HOPG, (b) a-axis HOPG, (c) diamond, and (d) HOPG with an average of a-axis and c-axis sound speeds. For all cases, the curves for Al and Ti are almost coincident.

In all cases, the calculated curves for Al and Ti are almost identical due to their similar speeds of sound. The average model is closer to matching the diamond model than either the c-axis or a-axis models. Since the experimental data for metal-graphite and metal-diamond systems is quite similar, it is possible that accounting for varying degrees of atomic scale roughness at the metal-graphite interface could explain the discrepancy shown in Fig. 3-5 between the standard DMM and the data.

Regardless of the treatment of in-plane and cross-plane phonon velocities in the graphite, the DMM still predicts a trend not supported by the data. The data shows Ti having much higher thermal interface conductance with HOPG than any of the other metals, and Al and Cr having comparable values of thermal interface conductance.

One possible explanation for this difference in trend is that the DMM does not account for adhesive forces or details in the bonding between the mediums. Young and Maris did lattice dynamics simulations that considered varying the spring constant at the interface between two dissimilar solids, and found that such variation had no appreciable effect on the transmissivity [62]. Stoner and Maris did lattice dynamics simulations to show that in the Pb-diamond system, the interfacial heat transport is limited by the speed at which energy can be transfered from the bulk Pb atoms to the interface atoms and between the interface atoms to the diamond [14]. Recently, Prasher adapted the acoustic mismatch model to account for adhesive energy at the interface, and found that the strength of adhesion in the case of van der Waals bonding at the interface is significant [19].

The observed film qualities as seen from the SEM images in Fig. 3-1 seem to correlate to the chemical interactions of the various metals with graphite. The wettability of carbon-based materials by metals had been studied extensively [57]. Gold, a nobel metal, does not wet carbon materials, while aluminum does, forming covalent bonds and carbide compounds. Transition metals like titanium and chromium bond strongly to carbon because carbon donates valance electrons to help fill the partially empty d-band. Titanium has stronger bonding than chromium because the bond strength is related to the number of available empty valance locations in the d-band. Also, Ti, like graphite has a hexagonal lattice structure, while the other metals studied have cubic structures. The similarity of the Al/Ti data to the pure Ti data also supports the idea that interfacial bonding could play an important role in the heat transport.

3.6 Graphite Transmissivity

We can use our measured results for G to extract phonon transmissivity values at metal-graphite interfaces using the DMM. If we make a best fit to our data for G with Eq. (3.6), using a sine dispersion relation, and allowing $\alpha_{1\rightarrow 2}$ to vary, we get the transmissivity value predicted by the DMM. These best fit curves are shown in Fig. 3-9. The fitted values for transmissivity are listed in Table 3.3. Also listed are transmissivity values obtained if a Debye dispersion relation is assumed, rather than a sine dispersion relation. The fits assuming a Debye relation are much worse and yield transmissivities roughly 2-3 times lower than assuming a sine dispersion. This emphasizes the importance of using a physically accurate dispersion relation, rather than a simple linear relation, at higher temperatures.

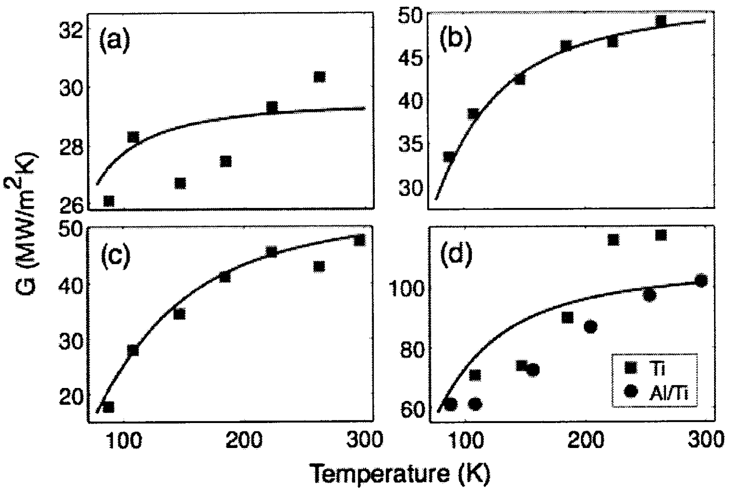

Figure 3-9: Best fit curves of measured G using Eq. (3.6) with a sine dispersion relation while allowing transmissivity to vary for (a) Au, (b) Al, (c) Cr, and (d) Ti and Al/Ti on HOPG. The predicted transmissivities are listed in Table 3.3.

Table 3.3: Phonon transmissivities at metal-graphtie interfaces obtained by fitting Eq. (3.6) to measured values of G. Results shown assuming both sine and Debye dispersion relations.

Dispersion:	Sine	Debye
Gold	0.061	0.023
Aluminum	0.032	0.013
Chromium	0.017	0.008
Titanium	0.067	0.027

3.7 Summary

Measurements of the thermal interface conductance between various metals and HOPG were made over a temperature range from 89 K to 300 K. Previous work has shown that this should provide a good approximation to the thermal interface conductance between metals and the sidewall of a MWCNT [53]. The results indicate that Ti-graphite interfaces have the highest conductance followed by Al/Ti, Al, Cr and Au.

We find that measurements of Al films with a 5 *nm* Ti stiction layer yield similar interface conductance results to Ti films, and have an improved signal-to-noise ratio for TTR measurements with a probe wavelength of 800 *nm*.

We also present room temperature results for the thermal interface conductance between HOPG and Ag, Ni and Sn. Plotting room temperature thermal interface conductance results between metals and HOPG as a function of the metal's Debye temperature shows a possible, albeit non-definitive, upward trend.

A comparison to published results for metal-on-diamond interfaces shows that metal-graphite and metal-diamond interface have similar thermal interface conductance values. This similarity may imply that a-axis graphite, c-axis graphite, and diamond all have similar values of G with metals. If so, the thermal interface conductance into the sidewall of a MWCNT may be similar to the thermal interface conductance with the end of the MWCNT.

We used the DMM, corrected for equivalent equilibrium phonon temperature, assuming a sine dispersion relation for the metal, and an effective two dimensional density of states in the graphite to serve as a comparison to our measured results. We find that assuming only c-axis phonon velocities in the graphite causes the DMM to drastically under predict the data. We suggest that atomic level roughness at the metal-graphite interfaces may have allowed some amount of phonon momentum to excite in-plane phonons in the graphite. By including equally weighted amounts of in-plane phonon velocities in addition to cross-plane phonon velocities, we achieve over-predictions of our data. We suggest that the degree of coupling depends on the metal deposited and that this coupling could provide an explanation for the under prediction using only c-axis velocities. Differences in adhesive forces or electronic interactions may also have contributed to the discrepancy.

We also use our measured results to extract phonon transmissivities at metal-graphite interfaces based on the DMM. The results and analyses presented here are useful for the characterization of MWCNTs as well as for the design of devices that utilize carbon-based nanostructures.

Chapter 4

Effects of Surface Chemistry on Thermal Conductance at Al-Diamond Interfaces

4.1 Motivation and Background

The motivation for this study grew from interest in both fundamental physics and practical application. From a fundamental perspective, our aim was to understand the contribution of surface chemistry to thermal interface conductance. Our sample system was single crystal diamond coated in a thin layer of aluminum. The diamond was functionalized with different surface terminations: either oxygen or hydrogen. Aluminum bonds differently to oxygen and hydrogen, and we were curious to uncover the effects, if any, on the thermal interface conductance. Interfacial bonding is not a parameter generally considered in models of interface conductance at solid-solid interfaces, except in the case of very weak interfacial bonds [19]. An experimental study of the effects of surface chemistry on the thermal interface conductance will complement further theoretical studies.

We were also motivated by practical application. Synthetic diamond has promise as a heat spreading material due to its exceptionally high thermal conductivity (around 2000 W/mK at room temperature). For use in the integrated circuit industry, diamond would have to be formed into a composite material with metal in order to mitigate thermal expansion issues [63, 64, 65]. Synthetic diamond also has potential as a possible transistor material due to its favorable electrical properties [66].

Many studies of the electrical properties, and in particular the surface conductivity, of diamond interfaces have been reported[67, 68, 69, 70, 71, 72, 73]. The surface termination of the diamond was found to have a significant impact on the surface electrical properties and on the interfacial electronic properties with various metals [70, 71, 72, 73].

Studies of metal-diamond adhesion have also indicated that surface termination influences adhesion strength [74, 75, 76, 77]. A correlation between adhesion strength and thermal interface conductance has been developed in the case of van der Waals interactions at the interface, and showed that adhesion energy is an important parameter [19].

Very few studies of the thermal interface properties between metal and diamond have been reported. Kappus and Weis (1973) studied Au, Cu, Ni and Pb films on (100) and (110) diamond. They held the diamond at liquid helium temperatures and used the metals as phonon radiators to study the relationship between radiation temperature and emitted phonon temperature per metal contact area [78]. Directly relating their results to thermal interface conductance, however is not straightforward. Stoner and Maris (1992) reported measurements of the thermal interface conductance between isotopically enriched diamond and Al, Au, Pb and Ti [54]. In addition, Lyeo and Cahill (2006) measured the thermal interface conductance between H-terminated diamond and Bi and Pb. Both Maris and Cahill used transient thermorefelctance measurement techniques. To our knowledge, no prior study of solid-solid thermal interface conductance that takes surface termination into account has ever been reported.

In this work, we study the thermal interface conductance between Al and four samples of single crystal diamond with varying surface terminations and impurity levels:

medium and low purity H-treated samples, and medium and low purity oxygenated samples.

4.2 Samples and Surface Characterization

The single crystal diamond samples used in this study were prepared by Apollo Diamond Inc. The samples were grown homo-epitaxially on diamond wafers and later removed from the wafers. All samples are of IIA purity, with nitrogen representing the primary impurity. For convenience, the designations "low purity" and "medium purity" are adopted to describe the nitrogen content of samples, where low purity samples contain approximately 1 *ppm* nitrogen, and medium purity samples contain approximately 0.1 *ppm* nitrogen.

The as-grown samples are natively hydrogen-terminated, but the as-grown diamond is very rough, and requires polishing. The samples were scaife polished on their (100) surfaces to have a root mean square surface roughness of approximately 20 *nm*. The polishing process disrupts the native surface termination, and thus each sample is treated after polishing to have a desired surface functionalization. One low purity and one medium purity sample were hydrogen treated by exposure to a hydrogen plasma at 700°C [79]. Another low purity and medium purity sample were oxygen treated by being heated in air at 500°C [80].

A qualitative view of the achieved functionalization may be gained by observing the contact angle of water with the surface. An oxygen terminated surface is more hydrophilic, while a hydrogen terminated surface is more hydrophobic [81]. Figure 4-1 shows the results of a goniometer measurement of the contact angle of deionized water (DI) to the (100) polished sample surfaces. The contact angles clearly show that the oxygenated samples are more hydrophilic, while the H-treated samples are more hydrophobic. In addition, the contact angles suggest that the surface treatments had similar effects on both the high purity and medium purity samples.

A more quantitative analysis of the surface functionalization was done through x-ray photoelectron spectroscopy (XPS). The measurement was done on a Kratos

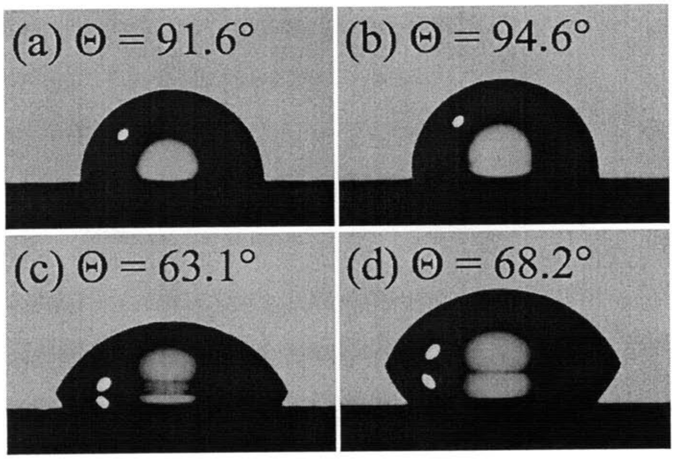

Figure 4-1: Contact angle of DI water on (100) polished surfaces of (a) H-treated low purity, (b) H-treated medium purity, (c) oxygenated low purity, and (d) oxygenated medium purity single crystal diamond samples.

AXIS Ultra Imaging X-Ray Photoelectron Spectrometer with the beam at normal incidence to the surface. The results, shown in Table 4.1, give the concentration percentage of atoms within the first few atomic layers near the surface. XPS is not capable of detecting light atoms like hydrogen, making the amount of hydrogen on the surface less quantifiable. It is possible, however, to make a comparison of the amount of oxygen near the surface. The oxygenated samples have roughly 5 to 7 times more oxygen near their surfaces than the H-treated samples. The trace amounts of molybdenum and silicon may have resulted from the polishing process, and the trace amount of sulfur may have resulted from some acid cleaning steps used after polishing.

Table 4.1: XPS measured atomic concentrations within the first few atomic layers of the sample surfaces. Note that XPS cannot detect the concentrations of light elements like hydrogen.

diamond sample	atomic concentration (%)
H-treated low purity	99.21 C, 0.54 O, 0.11 Mo, 0.14 Si
H-treated medium purity	98.90 C, 0.84 O, 0.08 Mo, 0.18 Si
oxygenated low purity	95.93 C, 4.00 O, 0.06 S
oxygenated medium purity	95.88 C, 4.05 O, 0.07 S

Together with the water contact angle results, the XPS measurement suggests that the oxygenated samples have a higher degree of oxygen terminated bonds, and that the surface chemistries are similar for the medium and low purity samples with the same surface treatments.

4.3 Thermal Interface Conductance Results

4.3.1 Experimental Details

After surface characterization, the samples were sputter coated with an 80 nm aluminum film at a pressure of 3 $mTorr$ and a deposition rate of 1 $\mathring{A}/s$. The thickness of the Al film was evaluated using acoustic echos off the Al-diamond interface. Because Al and diamond have a large acoustic mismatch, many echos were observed as shown in the inset of Fig. 4-2. The film thickness was also confirmed by comparison to a sample of single crystal sapphire, for which the thermal conductivity is known, that was sputter coated simultaneously with the diamond. Both methods yielded comparable results.

For the transient thermorefelctance measurement, a pump spot size of 60 μm, much larger than the probe spot size of 10 μm, was used to minimize the effects of radial conduction. The modulation frequency of the pump was 5.8 MHz. Measurements were conducted over a temperature range from 88 K to 300 K. Figure 4-2 compares typical room temperature thermoreflectance signals for H-terminated and oxygenated samples. The shape of the decay curve shows a marked difference for H-treated and oxygenated diamond samples. This difference in decay results from a difference in the thermal conductance at the Al-diamond interface.

Due to the extremely high thermal conductivity of diamond, we found our TTR measurement was more sensitive to the thermal interface resistance than to the diamond thermal conductivity. The interface represented a large resistance to heat flow compared to the conduction resistance in the diamond.

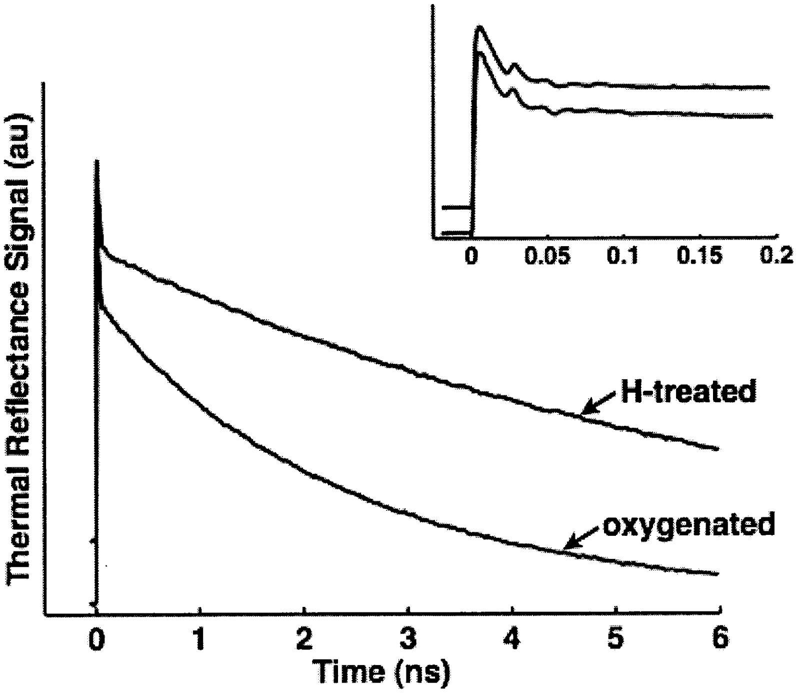

Figure 4-2: Typical scaled TTR signals at room temperature for H-treated and oxygenated samples. The inset shows the first 200 *ps* of data in which acoustic echos off the Al-diamond interface are apparent.

4.3.2 Results and Discussion

The average measured thermal interface conductance values as a function of temperature for each of the four samples is plotted in Fig. 4-3. The measured data's deviation from average was generally less than ±10%. The previously reported results of Stoner and Maris for Al-diamond thermal interface conductance are shown [54]. In addition, the prediction of the diffuse mismatch model using Eqs. (1.10) and (1.16) is shown for comparison.

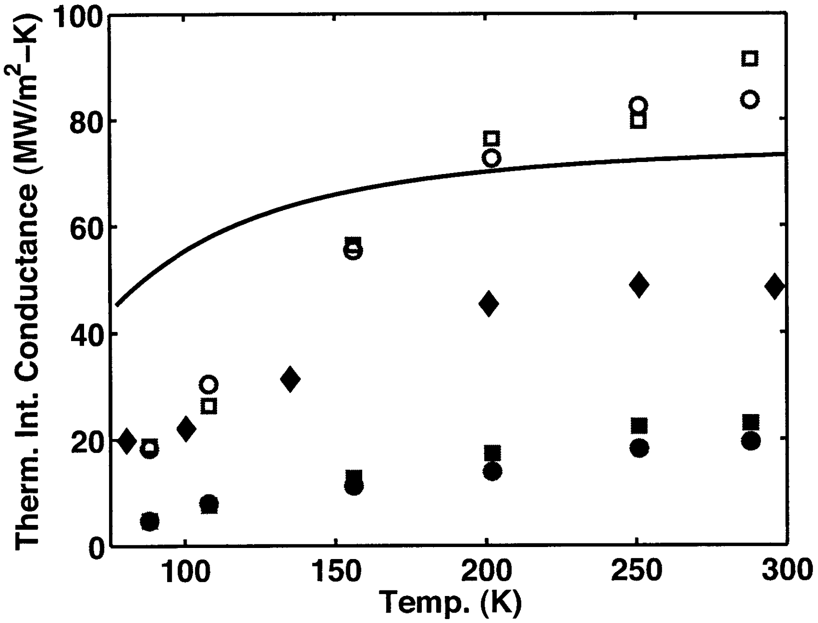

Figure 4-3: Measured thermal interface conductance between Al and H-treated low purity (closed circles), H-treated medium purity (closed squares), oxygenated low purity (open circles), and oxygenated medium purity (open squares) single crystal diamond samples. Previously reported results for Al-diamond thermal interface conductance values are shown as closed diamonds [54]. The solid line shows the prediction of the diffuse mismatch model.

The measured thermal interface conductance values are in the same range as those reported by Stoner and Maris [54], although the surface chemistry of the diamond studied by Stoner and Maris is unknown. Diamond surface chemistry clearly influences conductance. The oxygenated samples show roughly four times higher thermal interface conductance than the H-treated samples over the entire temperature range.

Also, the medium purity and low purity samples of each surface treatment gave comparable results. This similarity confirms the results of the XPS and water contact angle measurements that the achieved surface treatments were similar for each purity level.

While it is clear that surface chemistry effects heat transport at Al-diamond interfaces, the underlying mechanism is still unclear. Diamond is a dielectric, so electrons should be less influential to heat transport. The shape of the initial 200 *ps* peak in the thermoreflectance curve shown in Fig. 4-2 is similar for both H-treated and oxygenated samples, suggesting that the initial hot electron relaxation had little difference based on surface chemistry of the diamond.

We propose two possible mechanisms for the observed difference in interfacial heat transport: differences interfacial bonding and differences in Al grain structure. Aluminum bonds more strongly to oxygen than to hydrogen. This difference in bonding strength would result in a different elastic stiffness at the interface which could influence phonon transport, although further theory work is required to confirm such an influence for the case of strong bonding interactions.

Another possible mechanism for the observed difference in transport is a potential difference in the Al grain structure at the interface. The surface energy of oxygenated diamond is different from that of H-treated diamond, as indicated by the differences in water contact angle shown in Fig. 4-1. When metal is sputter deposited onto a surface, the formation of the metal film could be influenced by the surface energy mismatch of the metal and the deposition surface. If the Al film formed with dramatically different grain structures at the Al-diamond interface depending on the diamond surface termination, a difference in the available phonon states in the Al could have resulted in the observed difference in interfacial heat transport.

4.4 Investigations of Al Grain Structure

In order to investigate the possible influence of Al grain structure on the heat transport, several characterizations of the Al film were carried out. Figure 4-4 shows scanning electron microscope (SEM) images of the surface of the Al film on H-treated and oxygenated medium purity diamond.

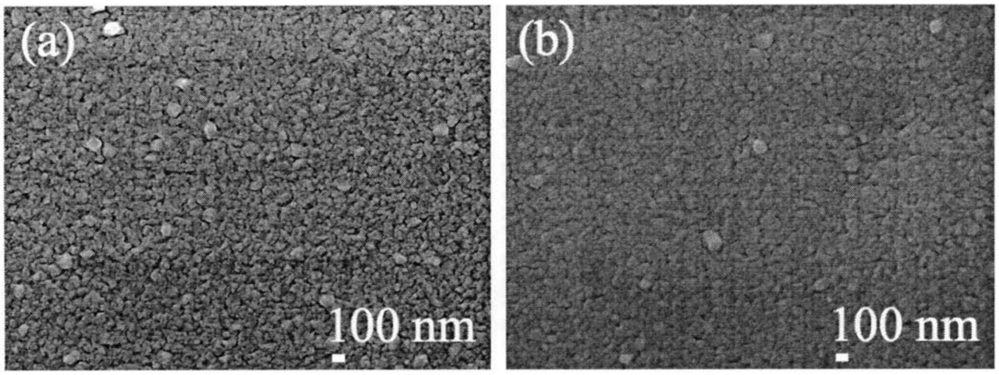

Figure 4-4: SEM images of Al film on (a) H-treated medium purity diamond and (b) oxygenated medium purity diamond.

The images do not indicate any clear difference between the Al films on the H-treated and oxygenated samples. For both, the Al film has grains on the order of 100 *nm*, which is comparable to the film thickness. A further study of film roughness was carried out using an atomic force microscope (AFM), as shown in Fig. 4-5. The scanning area for the AFM measurement was 1 *μm* x 1 *μm*. The AFM results indicate a roughness of approximately 20 *nm* on the surface of the Al film.

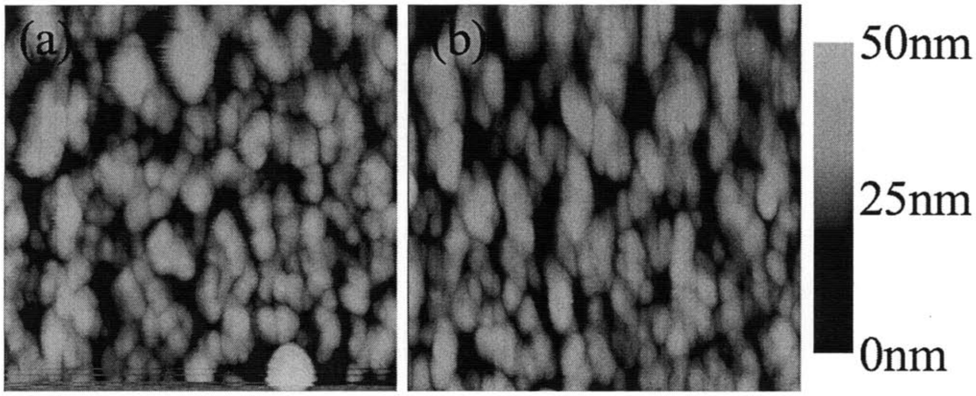

Figure 4-5: AFM images of Al film on (a) H-treated medium purity diamond and (b) oxygenated medium purity diamond. The scanning area was 1 *μm* x 1 *μm*.

While surface analyses cannot definitively indicate the Al grain structure at the

Al-diamond interface, they provide some useful insight. Since the thickness of the Al film is a mere 80 *nm*, and the grain size is on the order of 100 *nm*, it is possible that the surface of the film could be a reasonable indicator of the underlying film structure. To image the grain structure at the Al-dimaond interface, focused-ion-beam (FIB) microscopy was used as shown in Fig. 4-6

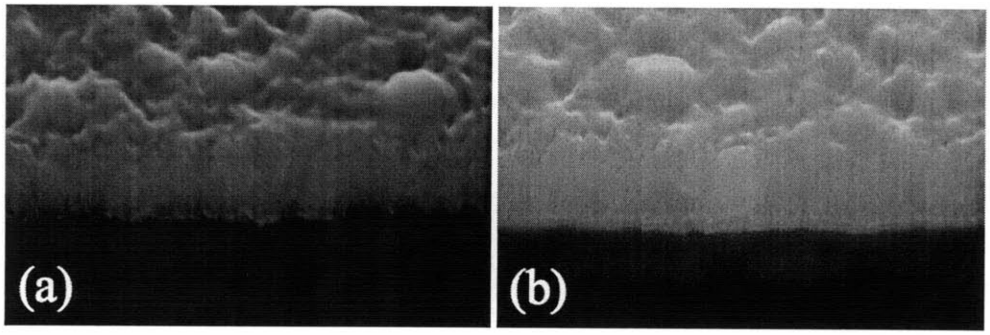

Figure 4-6: FIB microscopy images of Al film grain structure at the interface with (a) H-treated medium purity diamond and (b) oxygenated medium purity diamond. Darker region is diamond and lighter region is Al.

The FIB images reveal that the underlying grain structure of the Al on both H-treated and oxygenated diamond samples is similar. Both have a thin region of distinctly different structure near the interface that is approximately 15 percent of the total film thickness. Beyond this initial thin layer, a distribution of large and small grains is apparent, but no clear difference exists to distinguish the Al grain structure based on the diamond surface termination.

In order to produce a factor of four difference in thermal interface conductance, the microstructure of the Al film would need to be significantly different for oxygenated and H-treated samples. SEM, AFM and FIB microscopy all suggest that the microstructure of the Al film is not a strong function of the diamond surface termination. Consequently, differences in interfacial bond strength, rather than film microstructure, likely resulted in the observed difference in thermal interface conductance between H-treated and oxygenated diamond samples.

4.5 Summary

We find that diamond surface chemistry has a significant impact on interfacial heat transport at Al-diamond interfaces. Interfaces of Al with oxygenated diamond show roughly four times higher conductance that interfaces of Al with H-treated diamond. No prior experimental study of solid-solid thermal interface conductance has considered the influence of surface chemistry.

The mechanism for the difference in heat transport is not completely clear and merits further experimental and theoretical investigations. SEM and AFM surface imaging as well as FIB microscopy of the Al-diamond interface all showed no obvious difference in the Al grain structure based on diamond surface treatment. Thus, it seems probable that differences in interfacial bond strength produced the observed difference. The possible effects of interfacial bonding are not captured in current models of solid-solid thermal interface conductance in the case of strong bonding, and could lead to further insight into the physics of interfacial heat transport. Furthermore, we expect that the effects observed here are not limited to the Al-diamond system. From a practical perspective, the results of this study suggest that surface functionalization could provide a simple way to taylor thermal interface conductance.

Chapter 5

Conclusion

5.1 Summary

We have presented two experimental studies of thermal interface conductance at solid-solid interfaces conducted using pump and probe transient thermoreflectance (TTR) techniques. Each study hints at complex interfacial scattering phenomena that are not well captured by current theories of phonon transmissivity. We have also provided an overview of the classical theory of thermal interface conductance, as well as the TTR experimental method.

The first study considered interfaces of metal with highly ordered pyrolytic graphite (HOPG). The diffuse mismatch model (DMM), only accounting for phonon velocities in the cross-plane direction of graphite, tended to under predict the measured data, which lead us to hypothesize that atomic-scale roughness at the interface may have allowed for some degree of coupling to in-plane phonons in graphite. Due to graphite's extreme anisotropy, evan a small amount of coupling to the high velocity in-plane phonons of graphite causes a notable upward shift in the predicted conductance. We also propose that the degree of atomic-scale roughness would depend on the type of metal deposited and specifics of how the film formed. Using our measured results for thermal interface conductance, we also calculated the transmissivity of phonons at the interface as predicted by the DMM. The measured values of thermal interface conductance were similar to previously reported values for metal-on-diamond, which further supports the possibility of coupling to in-plane phonons. From a practical perspective, the similarity between metal-graphite and metal-diamond thermal interfaces may suggest that the conductance between metal and the c-axis of multi-walled carbon nanotubes (MWCNTs) could be similar to the conductance between metal and the a-axis of MWCNTs. Consequently, the results of this study could provide valuable input that would help to resolve problems with the unknown contact resistance inherent in measurements of the thermal properties of MWCNTs and other nanoscale carbon systems like graphene.

The second study considered interfaces of aluminum and single crystal diamond, where the diamond samples had variations in surface termination. The measured thermal interface conductance was found to be a strong function of the diamond surface termination, with oxygenated hydrophilic samples showing a factor of four higher conductance than hydrogen-treated hydrophobic samples. The mechanism for this observed difference could originate from differences in chemical bonding at the interface or from differences in the microstructure of the Al film. Aluminum bonds more strongly to oxygen than to hydrogen, but similarly it is possible that the sputtered Al film would form differently based on the mismatch in the surface energies created by the different chemical terminations. The microstructure of the film was investigated by scanning electron microscope (SEM) and atomic force microscope (AFM) surface imaging as well as by focused-ion-beam (FIB) imaging of the Al-diamond interface, and in all cases no obvious difference in the Al grain structure was observed based on diamond surface termination. Thus, differences in interfacial bond strength likely resulted in the observed difference in thermal interface conductance, but further theory work is needed to confirm this phenomenon. A model to incorporate adhesion energy into the acoustic mismatch model in the case of van dar Waals bonding at the interface has been developed [19], but no such analytical model considers stronger bonding interactions or extends the DMM. On the practical side, functionalizing diamond could provide a simple way to engineer thermal interface resistance.

Current models of thermal interface conductance largely fail to adequately explain experimental measurements, making experimental investigations of thermal interface conductance especially valuable for advancing the field. The studies presented here suggest possible directions for future theory and experimental work.

5.2 Future Work

To further explore the influence of metal film microstructure on thermal interface conductance, we plan to conduct an investigation in which the grain structure of the film is specifically engineered. One simple way to engineer film grain structure is through annealing. A single crystal wafer of an insulating material could be coated in a metal that will not diffuse into the wafer at elevated temperatures. The wafer should be insulating to eliminate uncertainties pertaining to electrons possibly contributing to transport, and the wafer should be single crystal to avoid any restructuring of its crystal structure upon annealing. The wafer could then be broken into sections and each section could be subjected to a different degree of annealing treatment. The thermal interface conductance of these samples measured through TTR techniques should provide a clear picture of the influence of the metal grain structure on the interfacial heat flow.

Further modeling work to advance current models of thermal interface conductance will also be considered in conjunction with carefully designed experiments that isolate individual factors that might influence conductance. The influence of electrons, both through electron-phonon coupling in the metal and through electron-phonon and electron-electron coupling at the interface should be explored further, but isolating their influence in a controlled experimental way could prove challenging.

Bibliography

[1] E. T. Swartz and R. O. Pohl. Thermal boundary resistance. *Rev. Mod. Phys.*, 61(3):605–668, Jul 1989.

[2] W. A. Little. The transport of heat between dissimilar solids at low temperatures. *Canadian Journal of Physics*, 37:334–+, 1959.

[3] M.G. Cooper, B.B. Mikic, and M.M. Yovanovich. Thermal contact conductance. *International Journal of Heat and Mass Transfer*, 12(3):279 – 300, 1969.

[4] G. L. Pollack. Kapitza resistance. *Rev. Mod. Phys.*, 41(1):48–81, Jan 1969.

[5] P. L. Kapitza. Heat transfer and superfluidity of helium ii. *Phys. Rev.*, 60(4):354–355, Aug 1941.

[6] G. Chen and T. Zeng. Nonequilibrium phonon and electron transport in heterostructures and superlattices. *Nanoscale and Microscale Thermophysical Engineering*, 5(2):71–88, Apr 2001.

[7] J. A. Katerberg, C. L. Reynolds, and A. C. Anderson. Calculations of the thermal boundary resistance. *Phys. Rev. B*, 16(2):673–679, Jul 1977.

[8] I. M. Khalatnikov. Discontinuities and large amplitude sound waves in helium ii. *Zh. Eksp. Teor. Fiz.*, 22:687, 1952.

[9] E. T. Swartz and R. O. Pohl. Thermal resistance at interfaces. *Appl. Phys. Lett.*, 51(26):2200–2202, Dec. 1987.

[10] P. Reddy, K. Castelino, and A. Majumdar. Diffuse mismatch model of thermal boundary conductance using exact phonon dispersion. *Applied Physics Letters*, 87(21):211908, 2005.

[11] J. C. Duda, J. L. Smoyer, P. M. Norris, and P. E. Hopkins. Extension of the diffuse mismatch model for thermal boundary conductance between isotropic and anisotropic materials. *Applied Physics Letters*, 95(3):031912, 2009.

[12] C. Dames and G. Chen. Theoretical phonon thermal conductivity of si/ge superlattice nanowires. *Journal of Applied Physics*, 95(2):682–693, 2004.

[13] N. S. Snyder. Heat transport through helium ii: Kapitza conductance. *Cryogenics*, 10(2):89 – 95, 1970.

[14] R. J. Stoner and H. J. Maris. Kapitza conductance and heat flow between solids at temperatures from 50 to 300 k. *Phys. Rev. B*, 48(22):16373–16387, Dec 1993.

[15] H. K. Lyeo and D. G. Cahill. Thermal conductance of interfaces between highly dissimilar materials. *Phys. Rev. B*, 73(14):144301, Apr 2006.

[16] D. G. Cahill, W. K. Ford, K. E. Goodson, G. D. Mahan, A. Majumdar, H. J. Maris, R. Merlin, and S. R. Phillpot. Nanoscale thermal transport. *Journal of Applied Physics*, 93(2):793–818, 2003.

[17] P. E. Hopkins, P. M. Norris, and R. J. Stevens. Influence of inelastic scattering at metal-dielectric interfaces. *Journal of Heat Transfer*, 130(2):022401, 2008.

[18] P. E. Hopkins and P. M. Norris. Relative contributions of inelastic and elastic diffuse phonon scattering to thermal boundary conductance across solid interfaces. *Journal of Heat Transfer*, 131(2):022402, 2009.

[19] R. Prasher. Acoustic mismatch model for thermal contact resistance of van der waals contacts. *Applied Physics Letters*, 94(4):041905, 2009.

[20] A. Majumdar and P. Reddy. Role of electron–phonon coupling in thermal conductance of metal–nonmetal interfaces. *Applied Physics Letters*, 84(23):4768–4770, 2004.

[21] K. H. Yoo and A. C. Anderson. Thermal impedance to normal and superconducting metals. *J. Low Temp. Phys.*, 63(3/4):269–286, 1986.

[22] J. G. Fujimoto, J. M. Liu, E. P. Ippen, and N. Bloembergen. Femtosecond laser interaction with metallic tungsten and nonequilibrium electron and lattice temperatures. *Phys. Rev. Lett.*, 53(19):1837–1840, Nov 1984.

[23] R. M. Costescu, M. A. Wall, and D. G. Cahill. Thermal conductance of epitaxial interfaces. *Phys. Rev. B*, 67(5):054302, Feb 2003.

[24] P. M. Norris and P. E. Hopkins. Examining interfacial diffuse phonon scattering through transient thermoreflectance measurements of thermal boundary conductance. *Journal of Heat Transfer*, 131(4):043207, 2009.

[25] C. A. Paddock and G. L. Eesley. Transient thermoreflectance from thin metal films. *Journal of Applied Physics*, 60(1):285–290, 1986.

[26] W. S. Capinski and H. J. Maris. Improved apparatus for picosecond pump-and-probe optical measurements. *Review of Scientific Instruments*, 67(8):2720–2726, 1996.

[27] D. G. Cahill, K. Goodson, and A. Majumdar. Thermometry and thermal transport in micro/nanoscale solid-state devices and structures. *Journal of Heat Transfer*, 124(2):223–241, 2002.

[28] A. J. Schmidt. *Optical characterization of thermal transport from the nanoscale to the macroscale.* PhD thesis, Massachusetts Institute of Technology, 2008.

[29] T. Q. Qiu and C. L. Tien. Short-pulse laser heating on metals. *International Journal of Heat and Mass Transfer*, 35(3):719 – 726, 1992.

[30] T. Q. Qiu and C. L. Tien. Heat transfer mechanisms during short-pulse laser heating of metals. *Journal of Heat Transfer*, 115(4):835–841, 1993.

[31] T. Q. Qiu and C. L. Tien. Femtosecond laser heating of multi-layer metals–i. analysis. *International Journal of Heat and Mass Transfer*, 37(17):2789 – 2797, 1994.

[32] T. Q. Qiu, T. Juhasz, C. Suarez, W. E. Bron, and C. L. Tien. Femtosecond laser heating of multi-layer metals–ii. experiments. *International Journal of Heat and Mass Transfer*, 37(17):2799 – 2808, 1994.

[33] R. W. Schoenlein, W. Z. Lin, J. G. Fujimoto, and G. L. Eesley. Femtosecond studies of nonequilibrium electronic processes in metals. *Phys. Rev. Lett.*, 58(16):1680–1683, Apr 1987.

[34] S. D. Brorson, J. G. Fujimoto, and E. P. Ippen. Femtosecond electronic heat-transport dynamics in thin gold films. *Phys. Rev. Lett.*, 59(17):1962–1965, Oct 1987.

[35] S. Anisimov, B. L. Kapeliovich, and T. L. Perelman. Electron emission from metal surfaces exposed to ultrashort laser pulses. *Soviet Physics-JETP*, 39:375–377, Aug. 1974.

[36] W. S. Capinski, H. J. Maris, T. Ruf, M. Cardona, K. Ploog, and D. S. Katzer. Thermal-conductivity measurements of gaas/alas superlattices using a picosecond optical pump-and-probe technique. *Phys. Rev. B*, 59(12):8105–8113, Mar 1999.

[37] E. D. Palik, editor. *Handbook of Optical Constants of Solids.* Academic Press: New York, 1997.

[38] K. Ujihara. Reflectivity of metals at high temperatures. *Journal of Applied Physics*, 43(5):2376–2383, 1972.

[39] D. G. Cahill. Analysis of heat flow in layered structures for time-domain thermoreflectance. *Review of Scientific Instruments*, 75(12):5119–5122, 2004.

[40] A. J. Schmidt, X. Chen, and G. Chen. Pulse accumulation, radial heat conduction, and anisotropic thermal conductivity in pump-probe transient thermoreflectance. *Review of Scientific Instruments*, 79(11):114902, 2008.

[41] M. G. Burzo, P. L. Komarov, and P. E. Raad. Minimizing the uncertanties associated with the measurement of thermal properties by the transient thermoreflectance method. *IEEE Transactions on Components and Packaging Technologies*, 28(1):39–44, Mar. 2005.

[42] M. Polyanskiy. Refractive index database.

[43] J. C. Lambropoulos. From abrasive size to subsurface damage in grinding. *Optical Fab. and Testing*, 2000.

[44] J. C. Lambropoulos, Y. Li, P. Funkenbusch, and J. Ruckman. Non-contact estimate of grinding-induced subsurface damage. *Proc. SPIE*, 3782, 1999.

[45] P. Avouris. Carbon nanotube electronics. *Chemical Physics*, 281(2-3):429 – 445, 2002.

[46] A. Jorio. *Carbon Nanotubes: Advanced Topics in the Synthesis, Structure, Properties and Applications (Topics in Applied Physics)*. Springer, 1 edition, 2008.

[47] A. K. Geim and K. S. Novoselov. The rise of graphene. *Nat. Mat.*, 6:183–191, 2007.

[48] A. A. Balandin, S. Ghosh, W. Bao, I. Calizo, D. Teweldebrhan, F. Miao, and C. N. Lau. Superior thermal conductivity of single-layer graphene. *Nano Lett.*, 8(3):902–907, Feb. 2008.

[49] S. T. Huxtable, D. G. Cahill, S. Shenogin, L. Xue, R. Ozisik, P. Barone, M. Usrey, M. S. Strano, G. Siddons, M. Shim, and P. Keblinski. Interfacial heat flow in carbon nanotube suspensions. *Nat. Mat.*, 2:731–734, Oct. 2003.

[50] M. A. Panzer, G. Zhang, D. Mann, X. Hu, E. Pop, H. Dai, and K. E. Goodson. Thermal properties of metal-coated vertically aligned single-wall nanotube arrays. *Journal of Heat Transfer*, 130(5):052401, 2008.

[51] P. Kim, L. Shi, A. Majumdar, and P. L. McEuen. Thermal transport measurements of individual multiwalled nanotubes. *Phys. Rev. Lett.*, 87(21):215502, Oct 2001.

[52] M. Fujii, X. Zhang, H. Xie, H. Ago, K. Takahashi, T. Ikuta, H. Abe, and T. Shimizu. Measuring the thermal conductivity of a single carbon nanotube. *Phys. Rev. Lett.*, 95(6):065502, Aug 2005.

[53] R. Prasher. Thermal boundary resistance and thermal conductivity of multiwalled carbon nanotubes. *Phys. Rev. B*, 77(7):075424, Feb 2008.

[54] R. J. Stoner, H. J. Maris, T. R. Anthony, and W. F. Banholzer. Measurements of the kapitza conductance between diamond and several metals. *Phys. Rev. Lett.*, 68(10):1563–1566, Mar 1992.

[55] E. Pop, D. A. Mann, K. E. Goodson, and H. Dai. Electrical and thermal transport in metallic single-wall carbon nanotubes on insulating substrates. *Journal of Applied Physics*, 101(9):093710, 2007.

[56] H. Maune, H. Y. Chiu, and M. Bockrath. Thermal resistance of the nanoscale constrictions between carbon nanotubes and solid substrates. *Applied Physics Letters*, 89(1):013109, 2006.

[57] Y. J. Naidich. *Progress in Surface and Membrane Science.* Academic Press: New York, 1981.

[58] B. C. Gundrum, D. G. Cahill, and R. S. Averback. Thermal conductance of metal-metal interfaces. *Phys. Rev. B*, 72(24):245426, Dec 2005.

[59] C. Kittel. *Introduction to Solid State Physics.* Wiley: New York, 2005.

[60] J. L. Hostetler, A. N. Smith, D. M Czajkowsky, and P. M. Norris. Measurement of the electron-phonon coupling factor dependence on film thickness and grain size in au, cr, and al. *Appl. Optics*, 38(16):3614–3620, June 1999.

[61] Nuo Yang. Personal Correspondence, May 2010.

[62] D. A. Young and H. J. Maris. Lattice-dynamical calculation of the kapitza resistance between fcc lattices. *Phys. Rev. B*, 40(6):3685–3693, Aug 1989.

[63] K. Yoshida and H. Morigami. Thermal properties of diamond/copper composite material. *Microelectronics Reliability*, 44(2):303 – 308, 2004.

[64] P.W. Ruch, O. Beffort, S. Kleiner, L. Weber, and P.J. Uggowitzer. Selective interfacial bonding in al(si)-diamond composites and its effect on thermal conductivity. *Composites Science and Technology*, 66(15):2677 – 2685, 2006.

[65] J. Flaquer, A. Ríos, A. Martín-Meizoso, S. Nogales, and H. Böhm. Effect of diamond shapes and associated thermal boundary resistance on thermal conductivity of diamond-based composites. *Computational Materials Science*, 41(2):156 – 163, 2007.

[66] M. W. Geis. Diamond transistor performance and fabrication. *Proc. IEEE*, 79(5):669–676, 1991.

[67] Y. Mori, H. Kawarada, and A. Hiraki. Properties of metal/diamond interfaces and the effects of oxygen absorbed onto diamond surface. *Appl. Phys. Lett.*, 58(9):940–941, 1990.

[68] T. Tachibana, B. E. Williams, and J. T. Glass. Correlation of the electrical properties of metal contacts on diamond films with the chemical nature of the metal-diamond interface. ii. titanium contacts: A carbide-forming metal. *Phys. Rev. B*, 45(20):11975–11981, May 1992.

[69] P. K. Baumann and R. J. Nemanich. Characterization of copper-diamond (100), (111), and (110) interfaces: Electron affinity and schottky barrier. *Phys. Rev. B*, 58(3):1643–1654, Jul 1998.

[70] J. Ristein, F. Maier, M. Riedel, and J. B. Cui. Surface electronic properties of diamond. *Phys. Stat. Sol. (a)*, 181:65–76, 2000.

[71] M. Szameitat, X. Jiang, and W. Beyer. Influence of adsorbates on the surface conductivity of chemical vapor deposition diamond. *Applied Physics Letters*, 77(10):1554–1556, 2000.

[72] F. Maier, M. Riedel, B. Mantel, J. Ristein, and L. Ley. Origin of surface conductivity in diamond. *Phys. Rev. Lett.*, 85(16):3472–3475, Oct 2000.

[73] J. A. Garrido, A. Härtl, S. Kuch, M. Stutzmann, O. A. Williams, and R. B. Jackmann. ph sensors based on hydrogenated diamond surfaces. *Applied Physics Letters*, 86(7):073504, 2005.

[74] S. V. Pepper. Effect of electronic structure of the diamond surface on the strength of the metal-diamond interface. *J. Vac. Sci. Technol.*, 20(3):643–646, 1982.

[75] X. G. Wang and S. R. John. Copper/diamond adhesion and hydrogen termination. *Phys. Rev. Lett.*, 87(18):186103, Oct 2001.

[76] Y. Qi and L. G. Hector. Hydrogen effect on adhesion and adhesive transfer at aluminum/diamond interfaces. *Phys. Rev. B*, 68(20):201403, Nov 2003.

[77] Y. Qi and L. G. Hector. Adhesion and adhesive transfer at aluminum/diamond interfaces: A first-principles study. *Phys. Rev. B*, 69(23):235401, Jun 2004.

[78] W. Kappus and O. Weis. Radiation temperature and radiation power of thermal phonon radiators using diamond as transmission medium. *J. Appl. Phys.*, 44, 1974.

[79] P. W. May, J. C. Stone, M. N. R. Ashfold, K. R. Hallam, W. N. Wang, and N. A. Fox. The effect of diamond surface termination sepcies upon field emission properties. *Diam. Rel. Mat.*, 7:671–676, 1998.

[80] H. Gamo, K. Iwasaki, K. Nakagawa, T. Ando, and M. N. Gamo. Surface conductivity change by oxidation of the homoepitaxially grown diamond (100) surface. *J. Phys,: Conf. Ser.*, 61:322–335, 2007.

[81] C. G. Spect, O. A. Williams, R. B. Jackman, and R. Schoepfer. Ordered growth of neurons on diamond. *Biomaterials*, 25:4073–4078, 2003.